CARRIER DYNAMICS AT Si-DIELECTRIC INTERFACES STUDIED BY SECOND-HARMONIC-GENERATION

By

Wei Wang

Dissertation

Submitted to the Faculty of the

Graduate School of Vanderbilt University

in partial fulfillment of the requirements

for the degree of

DOCTOR OF PHILOSOPHY

in

Physics

December, 2000

Nashville, Tennessee

Approved by:

Professor Norman H. Tolk

Professor Royal Albridge

Professor Jim Davidson

Professor Sokrates Pantelides

Professor Tom Weiler

To my parents

ACKNOWLEDGMENT

I would like to express my gratitude to my advisor professor Norman Tolk for all of his encouragement and guidance throughout the course of this research, especially in the last two years. I would like to acknowledge the tremendous help I received from professor Gunter Lüpke during this research. I would like to thank the Graduate School at Vanderbilt University for providing the opportunity and financial support for my graduate study. This research was also supported financially by the Office of Naval Research.

I wish to express my appreciation to all those who helped me in a variety of ways to complete my research and the dissertation. I thank the members of the CMASS group, especially professor Royal Albridge, and Dr. Shailesh Singh, and Dr. Jonathon Gilligan, Ms. Jane Fall, and fellow students Michael Albert, Zsuzsa Marka, Christine Cheney, and Judit Sturmann. I would also like to thank Dr. Michael Budde and Dr. Sergey Rashkeev for many useful and interesting discussions. I would like to thank professor Gerald Lucovsky and Dr. David Wolfe at North Carolina state university for providing the $ZrSiO_x$ samples. I also thank Dr. I. Kizilyalli and Dr. P. K. Roy at Lucent Technologies for providing the Si/SiO_2 samples.

I would also like to thank all members of my PhD committee, Professor Royal Albridge, Professor Jim Davidson, Professor Sokrates Pantelides, and Professor Tom Weiler, who provided many useful advices.

TABLE OF CONTENTS

Appendices

LIST OF FIGURES

LIST OF TABLES

CHAPTER I

INTRODUCTION

With the rapid growth of the semiconductor industry, channel lengths in chips have been reduced drastically in recent years. Clearly, scaling laws require a reduction in the thickness of insulator layers as well. As a result, new issues arise such as electron tunneling and dopant migration, which may critically affect the performance and reliability of CMOS-based devices. [Feldman 1998] Many approaches have been tried in the last several years to address these issues. The incorporation of nitrogen at the Si/SiO_2 interfaces during the growth process was shown to reduce dopant migration significantly. [Hwang 1990] [Hattangady 1995] Later, high-K dielectrics were investigated as a possible replacement for silicon dioxide. [Campbell 1997] [Kizilyalli 1998] [Wilk 2000] This new class of materials was found to significantly reduce leakage current, which has been the most troubling problem for ultrathin SiO_2. More recently, various crystalline oxides have been considered to improve interface quality, and preliminary results look very promising. [McKee 1998]

With all these progresses made in dielectric materials growth on silicon, another issue also starts to attract attentions. How can we probe the atomic and electronic structures at the silicon-insulator interfaces? Traditional electrical methods require contacts. With insulator layers less than 100 Å, this task becomes more challenging. More importantly, electrodes have much more significant effects on the interfaces below ultrathin oxides (<70 Å). It is unclear to what extent traditional electrical methods (C-V, I-V, etc.) can still be used to characterize the interfaces. For instance, low-frequency C-V measurements cannot be used here due to high direct tunnel currents. Effects like this can greatly complicate the interpretation of results detected from the interfaces.

Optical measurements have the advantage of being contactless. They are also non-intrusive compared to ion-beam measurements. With the recent advances in ultrafast laser technology, intense, tunable lasers have been developed with high reliability. This greatly improved capability of a variety of nonlinear optical techniques in many areas. Among them

second-harmonic-generation (SHG) is being widely considered. For symmetry consideration, SHG is very sensitive to interfaces between materials with inversion symmetry. The technique yields rich information on electronic structures, local fields, symmetry, and carrier dynamics at the interfaces. [McGilp 1996] [Aktsipetrov 1999] It can also be used for *in situ* measurements. It is therefore a promising tool for the investigation of Si-dielectric interfaces.

In this dissertation, the first SHG measurements on Si/high-K dielectric interfaces will be presented. The data show features that are drastically different from the Si-SiO_2 system. A model is proposed which indicates this difference is due to different carrier dynamics and trapping mechanism at/near the interfaces as well as to differences in band gaps and offsets. Wavelength-dependent SHG measurements find the conduction band offset of about 2.8 eV at the Si-$ZrSiO_x$ interface. This is the first measurement of the band offset at the Si-$ZrSiO_x$ interface using any kind of technique. The results give strong supports to $ZrSiO_x$'s candidacy as a replacement for SiO_2 in future generation semiconductor devices.

I.1 A Review of Si-Dielectric System

Si is the second most abundant element in the earth's crust (25.7 mass %), only exceeded by oxygen (46.7 mass %). It is also arguably the most extensively studied elemental material on this earth, due to its pivotal role in modern technology.

Jons J. Berzelius is credited with the first isolation of silicon in 1824, in the form of amorphous silicon. He accomplished this by heating potassium with silicon tetrafluoride (SiF_4). Later in 1854, crystalline silicon was first prepared by Jacque Deville. Today although amorphous silicon (a-Si) is a promising material for photovoltaic devices, crystalline silicon (c-Si) is unquestionably the primary focus of research activity since it forms the foundation of the semiconductor industry. Crystalline silicon is also the focus of this dissertation.

Silicon has a diamond lattice structure. The lattice is face-centered-cubic (fcc) with a two-atom basis. From figure1.1 it can be seen as two interpenetrating fcc lattices displaced along the body diagonal of the cubic cell by one quarter the length of the diagonal. The coordination number, the number of nearest neighbors, is 4. The cube side is about 5.43 Å.

Si has an indirect band gap at 1.12 eV. An indirect band gap significantly curtails the luminescent efficiency because of the requirement of the involvement by phonons. Due to the small band gap, which is in the infrared range, silicon's usage in areas such as high-resolution

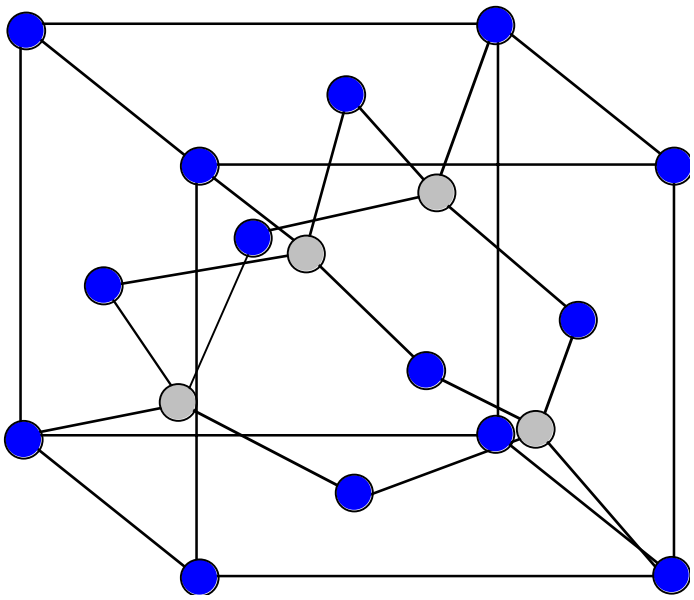

Figure 1.1 Atomic structure of crystalline Si

display is also doubtful. This makes silicon a less than desirable material for optical applications. The lowest direct interband transition, labeled E'_0 and located at the Γ point, is about 3.3 eV. It is almost degenerate with the E_1 transition at about 3.37 eV (figure 1.2), which is found along the Λ direction of the Brillouin Zone (BZ). These two direct band transitions play a significant role when nonlinear optical techniques are used to investigate silicon.

Intrinsic silicon, which has no appreciable dopants, has a conductivity of 3.16 μS/cm at room temperature. The electron mobility of silicon at room temperature is about 1450 $cm^2/V•sec$, while the hole mobility is about 480 $cm^2/V•sec$. Compared to those of some other semiconductors such as Ge (3900 $cm^2/V•sec$ for electrons, 1800 $cm^2/V•sec$ for holes) and GaAs (> 8000 $cm^2/V•sec$ for electrons), the numbers for carrier mobility in silicon are not large. This shows that intrinsically Si is not among the top candidates for many electrical applications.

Although both electrical and optical properties of silicon are less impressive than many other semiconductor materials, it has two huge advantages over them. The first is the low cost and relatively simple methods for processing crystalline silicon. The second is the extremely high quality of both the interface and bulk properties of the SiO_2 passivation layer.

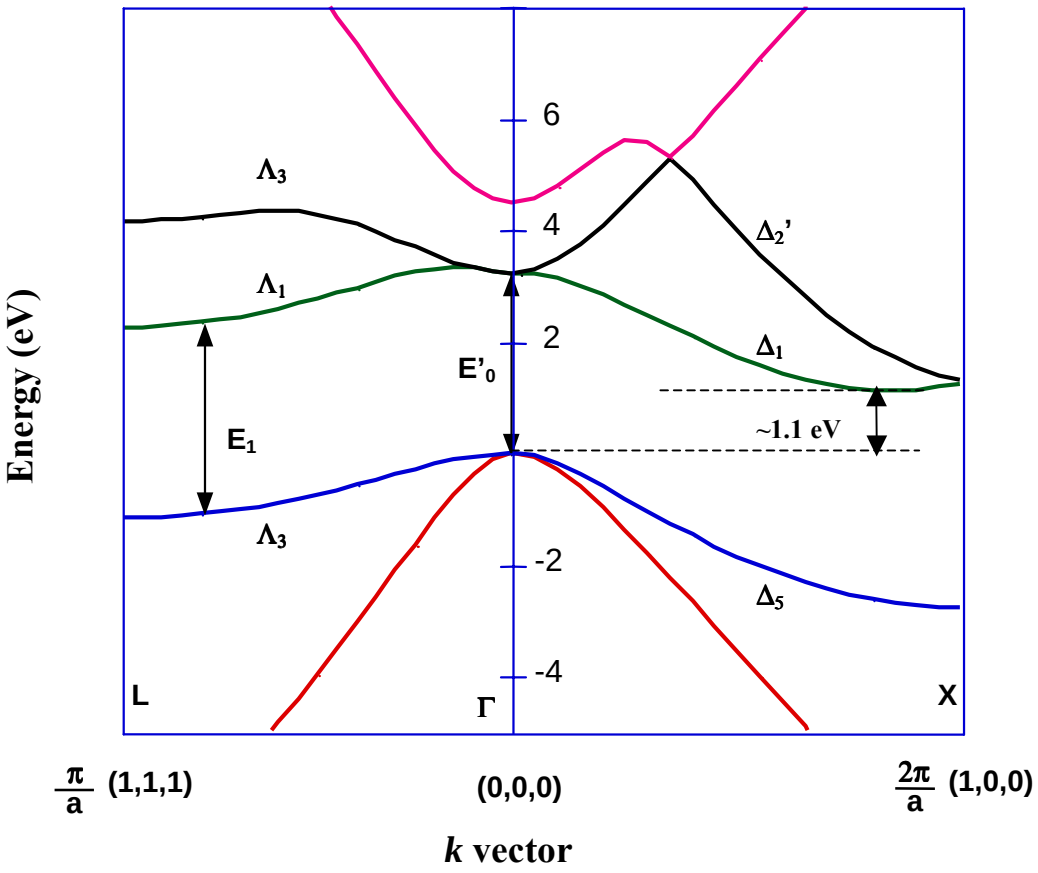

Figure 1.2 Band diagram of Si (100) calculated using Linear Muffin-Tin Orbital method (LMTO). Courtesy of S. N. Rashkeev.

Even twenty years ago, it was not difficult to make an electronic device from materials such as Ge and GaAs. However it is extremely difficult if one wants to make integrated circuits (IC), let alone large-scale-ICs (LSIC) out of these materials. To do so requires simplicity in architecture and processing technology as well as a high degree of device reliability. Due chiefly to the requirement of a high-quality insulator layer, most semiconductor materials except silicon are not suitable candidates for LSIC.

Metal-insulator-semiconductor (MIS) structures turn out to be the ideal device architecture combining simplicity and high-performance. But again it turns out that only metal-SiO_2-Si (MOS) structures fit the rigorous requirements of IC technology. The water-insoluble oxide film makes planar technology possible and permits fabrication of diffused or ion implanted

junctions with precisely controlled dimensions. Silicon dioxide is mechanically and chemically stable. As a passivation layer, it enables stable and predictable conditions at the semiconductor surfaces/interfaces to be manufactured during processing. It also screens devices from electrostatic effects caused by the ambient atmosphere. More importantly, an ideal gate insulator must have a large dielectric constant, low trap density at the interface, and a low density of bulk fixed charges. The Si/SiO_2 structure so far fulfills these requirements more perfectly than any other MIS structures. For example, films with bulk electron trap densities as low as $10^{16}/cm^3$ can be obtained. [Balk 1988] A schematic of a MOS-based field-effect-transistor (MOSFET) is shown in figure 1.3.

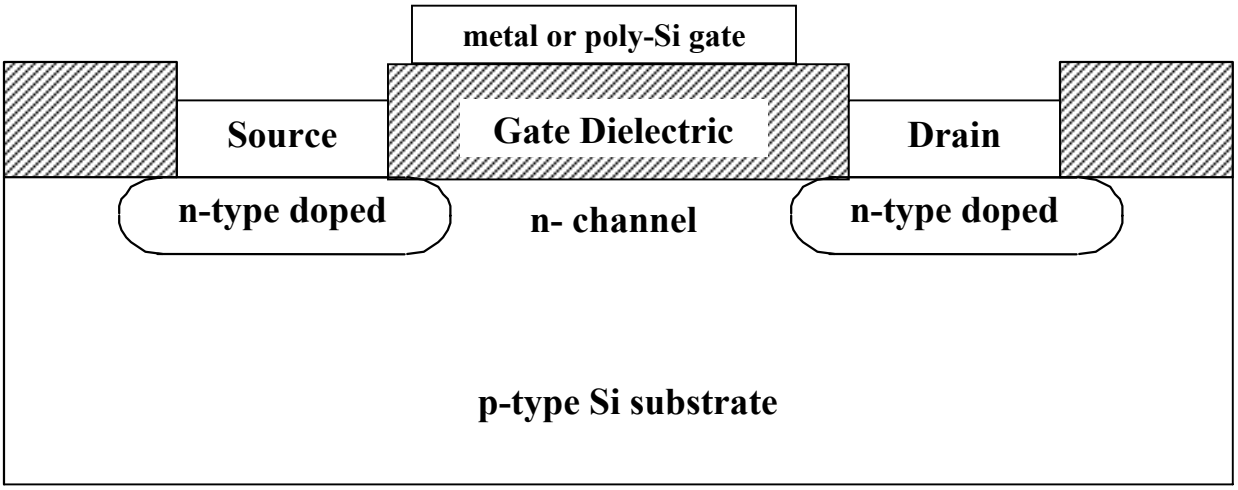

Figure 1.3 Schematic of an n-channel MOSFET

But in the last ten years the semiconductor technology has been growing rapidly and new challenges arise. The channel length in a MOSFET has decreased drastically and now is approaching sub-0.1-μm regime. This in turn requires gate oxide thickness to be scaled down to 30 Å, eventually to less than 10 Å. However at this dimension direct electron tunneling through SiO_2 film causes leakage current exceeding $1A/cm^2$ at ~1 V. This greatly degrades device performance and reliability. Furthermore, SiO_2 is not a good diffusion barrier against boron. Consequently, dopant (boron) diffusion into and through the SiO_2 layer from the poly-Si gate

becomes a critical issue. As a result, SiO_2 is not expected to be useful as a gate insulator for thickness below approximately 20 Å.

The operation of MOSFET depends on the charges generated in the channel at some given voltage. The total charge Q is the product of gate oxide capacitance and gate voltage. Therefore the crucial parameter for constant-field scaling is not the physical thickness, but instead the gate oxide capacitance per unit area:

$$C_{ox} = \varepsilon\varepsilon_0 / t_{ox} \quad \textbf{(1-1)}$$

ε is the dielectric constant of the material and t_{ox} is the physical thickness of the oxide. With physical oxide thickness t_{ox}, we can also define another important parameter, oxide equivalent thickness t_{ox-eq}, as:

$$t_{ox-eq} = \frac{t_{ox}\varepsilon_{SiO_2}}{\varepsilon} \quad \textbf{(1-2)}$$

where ε_{SiO_2} is the dielectric constant of silicon dioxide. Oxide equivalent thickness measures the thickness of the silicon dioxide layer, which yields the same capacitance as a material with dielectric constant ε and physical thickness t_{ox} does. Equation (1-2) shows that if a material with much higher ε than SiO_2 is employed, scaling laws can be maintained while thicker physical layers are still used for gate dielectrics.

As far back as the late sixties, there was a search for alternative dielectrics to replace SiO_2. Silicon nitride (Si_3N_4) has been at the top of this list from the beginning. The dielectric constant of Si_3N_4 is actually not much larger (7.0 for Si_3N_4, 3.9 for SiO_2). Therefore Si_3N_4 usually is not considered to be in the high-k (dielectric constant) materials category. Its small gain in the value of the dielectric constant is further complicated by its relatively small band gap (8.9 eV for SiO_2, 5.1 eV for Si_3N_4). This results in higher electron tunneling probability. The biggest advantage of the nitride is that it can form an effective deterrent against contaminant ion [Sze 1981] and dopant [Ito 1982] drift and therefore may be used as a barrier against boron diffusion in p^+ gate MOSFETs. However the Si/Si_3N_4 interface structure is of lower quality than the Si/SiO_2 interface. Bulk and interface trapping efficiencies in the Si_3N_4/Si system are several orders of magnitude larger than those in the SiO_2/Si system. [Balk 1988]

Knowledge of these two systems led to the concept of stack structures. The most successful structures are composed of layers of silicon dioxide and silicon nitride in the oxide/nitride (ON) and oxide/nitride/oxide (ONO) configurations. This spatially selective

incorporation of nitrogen atoms into the gate dielectric exhibits some significant new advantages. A small concentration of nitrogen near the interface appears to reduce hot-electron degradation and increases the threshold for electrical breakdown. MOSFETs utilizing the ON stack have achieved an equivalent oxide thickness of less than 20 Å. [Parker 1998] But two issues remain with regard to the silicon nitride system. The first is the high leakage current arising at low film thickness. The second is the relatively low quality interface between the silicon and the silicon nitride, leading for example to higher trap densities.

With regard to increased leakage current at low film thickness, currently the most popular approach is to use high-k dielectrics. With higher dielectric constant, the insulator thickness can increase accordingly while the capacitance of the insulator remains the same. Many materials in this category, including Al_2O_3, Ta_2O_5, TiO_2, Y_2O_3, CeO_2, ferroelectrics, ZrO_2 and HfO_2 are now being explored. [Feldman 1998] Table 1.1 shows some relevant properties of these materials. Close inspection of the properties of high-k dielectrics reveals a difficult challenge. Note that as the dielectric constant increases, the band gap of the material decreases. The inverse relationship between the band gap E_g and the dielectric constant ε can actually be shown by a semi-empirical equation [Stephen 1997]:

$$E_g \approx 20\left[\frac{3}{2+\varepsilon}\right]^2 \qquad \textbf{(1-3)}$$

This relationship means that in the effort to reduce tunneling current by using high-k dielectrics, gains made by increasing insulator thickness may be neutralized by the reduction in band offset, which enhances tunneling. But as long as the band gap and the barrier height are not too small, >4 eV for the band gap and >1 eV for the barrier height relative to Si, the advantage of using larger insulator thickness seems to outweigh the effect arising from the smaller band gap. It is therefore possible to find a material having a combination of physical thickness and a barrier height, which is superior to silicon in this regard.

But the challenges associated with a low-quality interface remain. MOS devices depend on the induction of charges in the channel resulting from the application of a voltage at the gate. This requires that the gate insulator and the interface between the insulator and the silicon be of very high quality. Fixed bulk charges and interface traps can pose serious problems for device performance and reliability. Traps can capture and release electrons or holes with various time constants. The presence of traps and the variety of trapping and detrapping lifetimes affect many

Table 1.1 Some important properties of metal oxides. After [Feldman 1998]

	MgO	Al_2O_3	SiO_2	TiO_2	Cr_2O_3	Y_2O_3	ZrO_2	Nb_2O_5	La_2O_3	CeO_2	HfO_2	Ta_2O_5	WO_3
Dielectric constant	8-10.5	10.5-12	3.5-4.1	80 167 [30]	9.2	14	[12 - 16]	50 30 35	20.8	21.2	[16] [45]	[25]	20 29
Band gap (eV)	7.3	8.8	9	3.05 2.59	4.8	2.1	2 3.95	1-3.2	5.4	3.4	 4.5	~5	2.2 - 2.5
Work function(ev)	3.1-4.4	4.8	5	3.9 6.2		2-3.9	3.1 – 5.8		2.8 – 4.2	3.2	2.8 3.75	4.6	
Density (g/cm3)	3.65	3.97	2.2 2.65 2.32	3.84 4.17 4.24	5.21	4.84	5.56 6.28	4.95	6.51	7.13	10.01	8.73	6.47
Heat of formation (106J/kg·mole)	602	1676	858 911	942 867	1130	1758		1906	1799	1089	1114	2047	841
Entropy (103J/kg·mole·deg)	27	51	42	50	81	124	50	136	153	74	59	143	62
Free energy of formation (106J/kg·mole)	-570	-1580	-805	-882	-1047	-1796	-1037	-1771	-1703	-971	-1080	-1970	-763
Melting point(K)	3073	2319	1993	2128	2573	2649	2963	1783	2573	2670	3063	2150	1743
Thermal conductivity at 373K/773K (W/m·deg)	27/8.8	30/9.1	1.6/	6.5/3.6			1.9/2.1						
Thermal expansion coeff. (10^{-6}/deg)	14-15	8	3 0.5	7-8	9.6	9.3	5-8		3.6 8.5	5.86 4			

device properties such as leakage current, capacitor storage time, threshold voltage and breakdown strength. The first MOS-like transistor was patented in 1935, but was not useful due to the charge trapping at the semiconductor surface. [Heil 1935] The success of Si/SiO_2 system is largely due to its ability to successfully meet this challenge.

Traps in the bulk are relatively easy to deal with. The presence of bulk traps is intimately related to the techniques used to grow the insulator films. In practice it is possible to grow near perfect insulator films with negligible bulk traps. But traps at the interfaces are more pervasive and more complicated as mismatch between two materials may pose intrinsic problems.

The SiO_2/Si system is distinguished by having an excellent interface. Although this interface is a transition between crystal silicon and a glassy material, silicon dioxide, it still has a remarkable degree of structural perfection. In SiO_2 the Si-O-Si bond energy changes very slowly as a function of bond angles and there can be rotation around the Si-O bond. Because of this flexibility, SiO_2 can form a glassy structure, often characterized as a continuous random network structure. Such a structure may be non-crystalline but still maintain completely saturated chemical bonds as shown in figure1.4. This same flexibility also makes it possible for the oxide

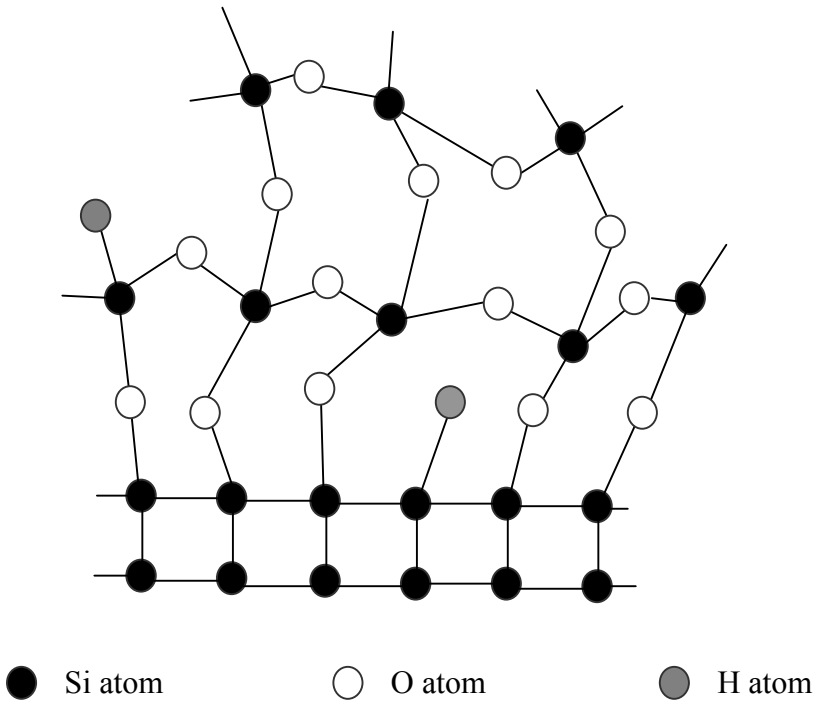

Figure 1.4 Si-SiO_2 interface structure

to adjust to the crystalline silicon and make saturated bonds at the interface. The remaining dangling bonds can be further saturated by hydrogen atoms. This is why one can obtain high quality Si/SiO_2 interface with a high degree of structural perfection. Defect densities as low as 10^{14}defects/m^2, corresponding to one defect for every 100,000 surface atoms, are often observed. [Svensson 1988] But so far neither nitride nor high-k materials have been able to achieve the same level of perfection at the interface.

One approach to this challenge for the high-k dielectrics is to add a very thin buffer layer of silicon oxide or oxynitride between the silicon substrate and the high-k dielectric. But this brings up a new question concerning the nature of the interface between the buffer layer and the high-k material. It also increases the complexity of the manufacturing process.

Recently an alternative method has been pursued to deal with these interface problems. In principle, by epitaxial growth of a suitable crystalline insulator on the silicon, one can obtain a perfect Si-insulator interface. This approach was first explored by growing crystalline CaF_2 on the Si (100) and (111) substrates. [Ishiwara 1982] [Fathauer 1984] However it was found that the lattice mismatch is not negligible (0.6%). [Fathauer 1984] More recently the possibility of depositing crystalline oxides on silicon (COS) has been proposed. In fact alkaline earth and perovskite oxides were grown in perfect registry with Si substrates. Combining the high-quality interface with the high dielectric constants of these oxides, a MOS capacitor with an equivalent oxide thickness of less than 10 Å was obtained. [McKee 1998] Still questions remain with regard to the compatibility of these techniques with the existing silicon processing techniques. And since most of the crystalline oxides are poly-crystalline, there may be problems with leakage current at the grain boundaries. Many electrical parameters also depend on crystal orientation. Poly-crystal oxides consequently may not achieve uniform device performance. But without doubt, crystalline oxides on silicon (COS) open a new, potentially revolutionary, path towards the next generation of silicon technology.

I.2 A Review of Second Harmonic Generation (SHG)

The first second harmonic generation (SHG) experiment carried out by Franken et al. in 1961 marked the birth of the field of nonlinear optics. [Franken 1961] Since then the effect has found wide applications as a means to extend coherent light sources to shorter wavelength. Then

in the early 80s, Shen's group in Berkeley established the potential of SHG as a surface probe and opened a new chapter for SHG applications. [Shen 1985]

Although quantum mechanics is required to have a full, quantitative understanding of second harmonic generation, the classic Lorentz model of the atom is sufficient to give a physical picture of this phenomenon. When light interacts with a medium, the electrons and ion cores are pulled away from each other, creating electric dipoles in the medium. The sum of the electric dipole moments gives rise to the polarization (**P**) of the material.

The motion of the ions is insignificant compared to that of the much lighter electrons. Therefore only the motion of electrons is considered in the Lorentz model. The equation of motion for the electron takes the form of

$$\ddot{\mathbf{x}} + 2\gamma\dot{\mathbf{x}} + \omega_0^2\mathbf{x} + (\mathbf{a}\mathbf{x}^2 + \mathbf{b}\mathbf{x}^3 + ...) = -\mathbf{e}\mathbf{E}(\mathbf{t})/\mathbf{m} \qquad \textbf{(1-4)}$$

where the electric field E(t) is assumed to have the form of $E_0\cos(\omega t)$ and γ is the damping constant. If one ignores the nonlinear terms ax^2, bx^3, … for the moment, equation (1-4) shows that the motion of electrons is of the form of a simple harmonic oscillation coupled with a force with optical frequency ω. An oscillating electric dipole can then radiate an electromagnetic field with the same frequency ω.

Simple harmonic oscillation holds only if the amplitude of the oscillation is small. This translates into a small incident electromagnetic field. But if the intensity of the light is high, the electromagnetic field will be large. This will result in anharmonic behavior of the dipole oscillation. The nonlinear terms ax^2, bx^3, … in equation (1-4) characterize the anharmonic oscillation of the dipoles. As shown in appendix A, the anharmonic potential will lead to higher order harmonic oscillations at frequencies 2ω, 3ω, and so on. This is analogous to the harmonic distortion of signals in an electrical circuit whose response is not linear. The oscillating electric dipoles then radiate field at the corresponding frequencies, which leads to second-, third-, … harmonic-generation.

Under this electric dipole approximation, the interaction between an electromagnetic (EM) field and condensed matter can be described by a general polarization. This polarization, $P(\omega, 2\omega, \ldots)$, induced by the EM field $E(\omega)$ with frequency ω, can be written as:

$$P_i = \chi_{ij}^{(1)} E_j + \chi_{ijk}^{(2)} E_j E_k + \chi_{ijkl}^{(3)} E_j E_k E_l + ... \qquad \textbf{(1-5)}$$

The first term describes the linear optical response. The other terms describe the nonlinear optical responses, which become significant when the EM field becomes large. Among these terms the lowest one is responsible for SHG. $\chi^{(2)}$ is called second order nonlinear susceptibility. It is a third rank tensor and describes the second-order nonlinear optical response from the medium.

In second harmonic generation both energy $\hbar\omega$ and momentum $\hbar\mathbf{k}$ have to be conserved. These conditions can be described as $\omega_2=2\omega_1$ and $\mathbf{k_2}=2\mathbf{k_1}$, where ω_1 and ω_2 are optical frequencies of the fundamental and second-harmonic beams, respectively, while $\mathbf{k_1}$ and $\mathbf{k_2}$ are the wave vectors of the fundamental and second-harmonic beams, respectively. The momentum conservation condition is also called the phase matching condition. It originates from the classical model. The physics can be best understood as follows. The polarization $P(\omega_2= 2\omega_1)$ is proportional to $E^2(\omega_1) \propto \exp(-i2k_1x)$. For two electric dipoles separated by a distance of d, there is a phase difference of $2k_1d$ in their polarizations. The second harmonic field generated by the first dipole, which is proportional to $\exp(-ik_2x)$, arrives at the second dipole with a phase difference of k_2d. If the second harmonic field generated by the second dipole is to be in phase with the SHG from the first dipole, the phase differences $2k_1d$ and k_2d, must be equal. This leads to the phase matching condition $\mathbf{k_2}=2\mathbf{k_1}$. In the classical model, this phase matching condition requires the radiations from all the electric dipoles to be in phase.

Since k is the wave vector of the beam, the momentum conservation condition also means that if the fundamental beam is collinear, the SHG beam will be collinear as well and at the same direction as the fundamental beam. This greatly simplifies the detection of SHG beams.

The penetration depth of optical radiation into semiconductors and insulators is relatively large. This makes it difficult to isolate surface/interface contributions from bulk contributions. However researchers quickly recognized that symmetry differences between the bulk and the interface/surface may readily be exploited. Resonance associated with interface states can also be exploited. The linear optical response of the interface usually provides little or no information on the crystalline structure of the interfacial layer since the linear-optical parameters are scalars in the most important cubic media. In contrast, the symmetry characteristics inherent in the higher-order optical susceptibilities, which are tensors, are indicative of the symmetry of the interfacial structure. Thus, second harmonic generation becomes a sensitive tool to investigate surface/interface structures. This technique offers several significant advantages over

conventional surface spectroscopies associated with charged particle beams such as electron beams and ion beams. By use of the contactless SHG technique, materials damage and contamination is eliminated; all pressure ranges are accessible; insulators can be studied without the problem of charging; and buried interfaces are readily accessible owing to the large penetration depth of the optical radiation. In addition, because the SHG technique is best used with an ultrafast laser, micrometer lateral resolution and femtosecond temporal resolution can be achieved easily.

Compared to traditional electrical methods, SHG still cannot quantitatively characterize a material under most circumstances. The advantage of being contactless can also become a disadvantage in some cases. Semiconductor devices usually have contacts on top of the oxide. After the contact is deposited, structural and electronic changes may take place underneath it. Therefore measurements taken on silicon with bare oxide may not reflect precisely the dynamics in a semiconductor device. Still the physics involved in a bare oxide system and a real device is very similar. Therefore SHG can still be a very effective tool for surface/interface studies, considering its strength mentioned earlier.

Initial surface SHG studies in the 1960s under non-ultra-high-vacuum (non-UHV) condition detected a surface signal, but found no dependence on adsorbate or surface structures. This held back the development of the field. An important breakthrough occurred in 1984 when the first SHG experiment under UHV condition was performed by Shen's group. [Tom 1984] These experiments showed that the adsorption of O and CO damped the SHG signals from Rh (111) while the adsorption of Na enhanced the signals. The following year Heinz showed that the azimuthal dependency of the SHG signal was sensitive to the symmetry change between the (2x1) and the (7x7) reconstructions of the Si (111) surface. [Heinz 1985] Later McGilp and Yeh used the Si(111)-Au system to show that SHG can provide structural information about buried interfaces. [McGilp 1986] Since then SHG has become a proven technique in investigating surface/interface structures. Among the materials studied, those with inversion symmetry, also referred as centrosymmetry, have gained particular attention.

The class of centrosymmetric materials includes many important materials such as metals and elemental semiconductors. Furthermore, under the electric dipole approximation it is easy to see that in the bulk, inversion symmetry leads to $\chi^{(2)}=-\chi^{(2)}=0$. At the surface however inversion symmetry is broken and the SHG contribution from the electric dipole is then allowed. This

makes SHG especially sensitive to the surface/interface structures of centrosymmetric materials. Among them the power of SHG is best illustrated by studies of silicon, which is centrosymmetric. Those studies show SHG is very sensitive to atomic symmetry, interfacial preparation and roughness, interface charge, applied electric fields, local resonance, strain, and crystalline oxide transition layers. [McGilp 1996]

Still precautions have to be taken when using SHG for interface/surface investigation. Although the SHG contribution from electric dipoles is forbidden in centrosymmetric materials, Terhune *et al.* observed SHG from bulk calcite, which is centrosymmetric. [Terhune 1962] Later SHG was also detected from bulk materials such as Ag, Au, Si, Ge *et al*. Further studies showed these SHG signals are contributed by higher order, non-local multipoles, i.e. magnetic dipole and electric quadrupole terms. If these terms are considered, the second order nonlinear polarization can be written as:

$$\mathbf{P}_{\mathbf{tot}}^{(2)}(2\omega) = \mathbf{P}^{(2)}(2\omega) - \nabla \bullet \overleftrightarrow{\mathbf{Q}}^{(2)}(2\omega) + \frac{\mathbf{c}}{\mathbf{i}2\omega}\nabla \times \mathbf{M}^{(2)}(2\omega) \qquad \textbf{(1-6)}$$

The first term in the right is from electric dipole, which vanishes in centrosymmetric materials. The second and third are contributions from electric quadrupole and magnetic dipole, respectively. Together they can be described by an effective polarization as:

$$P_i^{eff}(2\omega) = \chi_{ijkl}^{(3)} E_j(\omega)\nabla_k E_l(\omega) \qquad \textbf{(1-7)}$$

For cubic media, this equation can be further simplified to:

$$\begin{aligned} P_i^{eff}(2\omega) &= (\delta - \beta - 2\gamma)E_j(\omega)\nabla_j E_i(\omega) + \beta E_i(\omega)\nabla_j E_j(\omega) \\ &\quad + \gamma\nabla_i E_j(\omega)E_j(\omega) + \zeta E_j(\omega)\nabla_j E_i(\omega) \end{aligned} \qquad \textbf{(1-8)}$$

Where $\delta = 2\chi_{iiii}$,

$\beta = 2\chi_{iijj}$,

$\gamma = \chi_{ijij}$,

$\zeta = \delta - \beta - 2\gamma - 2\chi_{ijji}$.

Sipe and Shen both showed that as far as signal detection is concerned, one cannot totally separate the bulk SHG contributions from the surface SHG in centrosymmetric media. [Sipe 1987] [Guyot-Sionnest 1988] Shen also showed that this bulk contribution is at most the same order of magnitude as the surface contribution. Nevertheless this bulk contribution, even though it may be very small in magnitude, indicates that for centrosymmetric materials, second

harmonic generation is a sensitive tool for the investigation of structural changes at the surface rather than for the absolute determination and characterization of the surface structure. Fortunately in many cases it is sufficient to detect that a change of surface structure occurs. This can be readily achieved by using the second harmonic generation technique.

At about the same time that a bulk effect was observed from materials with inversion symmetry, Bloembergen *et al.* also noticed that SHG signals from Si would be greatly enhanced if a DC voltage were applied across the sample. [Lee, 1967] This electric-field-induced SHG (EFISH) later was also detected from other centrosymmetric materials. It can be described by:

$$P_i(2\omega) = \chi_{ijk}^{(3)} E_j(\omega) E_k(\omega) E_{dc} \qquad \textbf{(1-9)}$$

where $\chi^{(3)}$ is a third order bulk susceptibility with electric dipole origin. E_{dc} is a quasi-static electric field normal to the surface. This field breaks the inversion symmetry and makes it possible to have an SHG contribution from the bulk electric dipole. An externally applied voltage, as it was carried out in the original experiment, is the most direct way to generate this quasi-static field. One example is the gate voltage in a MOS system. Therefore EFISH is an alternative, contactless, non-electric method to investigate the MOS device response from the gate voltage. This quasi-static field can also be generated internally. For instance, traps at the silicon surface can create a static field across the surface. In addition carriers which may be trapped/detrapped at these sites can alter this built-in field. As a result EFISH can also provide electronic structure information at the surface/interface.

Since the 1980s, EFISH has developed into a powerful tool to investigate surface/interface structure. It is also the main experimental method utilized in the work describe in this dissertation. EFISH is used to study both Si-SiO_2 system and Si-high-k system. There will be a more detailed discussion of EFISH and its application later in this work.

The remainder of this dissertation consists of three sections. In chapter II the experimental configuration is described, including the building and characterization of the principle experimental equipment: a Ti:Sapphire laser. In chapter III experimental results are presented along with relevant theories. The physical significance of these results is also discussed in that chapter. The last chapter summarizes the work and presents plan for future research.

CHAPTER II

INSTRUMENTATION AND EXPERIMENTAL SETUP

Since second harmonic generation is a nonlinear optical process, it strongly depends on the intensity of the excitation source. It is no coincidence that the progress in second harmonic generation studies is correlated with the development of lasers.

Ultrafast pulsed lasers are the preferred excitation source compared to continuous wavelength (CW) lasers. Even with a moderate average power, a pulsed laser can still have a very high peak power depending on its pulse width. For a CW laser to have power comparable to a pulse laser's peak power, a very high average power is required. Under many circumstances, this may complicate the experiment, or even damage the materials. On the other hand, pulsed lasers, especially ultrafast lasers with short irradiation duration, can generate nonlinear optical effects without the complication of local heating. This is especially crucial when SHG is used for spectroscopic purposes.

The search for reliable pulsed lasers, which should also be easy to operate and maintain, therefore became a major task in the development of SHG as a spectroscopic tool. Nd:(YAG, YAP, YLF) lasers and dye lasers were among the early approaches to pulsed laser operation. The breakthrough came in early 1990s with the invention, and then commercial availability, of the Ti: Sapphire laser. This laser provides a compact, powerful, ultrafast and easy to operate excitation source. The Ti:Sapphire laser is also the light source used in this thesis work. A large part of this dissertation work was the construction and characterization of a Ti:Sapphire laser.

II.1 The Construction of a Ti: Sapphire Laser

The Ti: Sapphire laser is a new class of solid-state laser developed in the early 1990s. It has a wide tunable wavelength range of about 400 nm and an ultra-short pulse width (<100 fs). Since its appearance the Ti: sapphire laser has become the most widely used tunable solid-state pulsed laser. Its success is largely due to two factors: the superb properties of the Ti: Sapphire nonlinear crystal and the application of the mode-lock technique to this laser system.

In most lasers, all energy released via stimulated emissions by the exited medium is in the form of photons. However in some solid-state lasers, the stimulated emission of photons is coupled to the emission of phonons in the crystal lattice. In these lasers, although the total energy of the inter-state transition is fixed, the released energy can be partitioned between photons and phonons in a continuous fashion. This coupling leads to broad band emission, which enables the wavelength tunability of these lasers.

The energy-level structure of sapphire (Al_2O_3) doped with titanium (Ti) is shown in figure 2.1. The ground state, a $^2T_2$ state, has a broad sequence of overlapping vibrational or vibronic levels extending upwards from the lowest level. The first excited state is a ^2E state that also extends upwards with a series of overlapping vibronic levels. Excitation occurs from the lowest vibronic level of the $^2T_2$ ground state to the broad range of excited vibronic levels of the ^2E excited state. The population pumped to these excited levels rapidly relaxes to the lowest level of the ^2E state. It then decays back to any one of the vibronic levels of the ground state with the emission of photons.

Due to this broad emission band Ti:Sapphire has a broad tuning range from 680nm to 1100nm. It has exceptional chemical stability and mechanical rigidity. Its high thermal

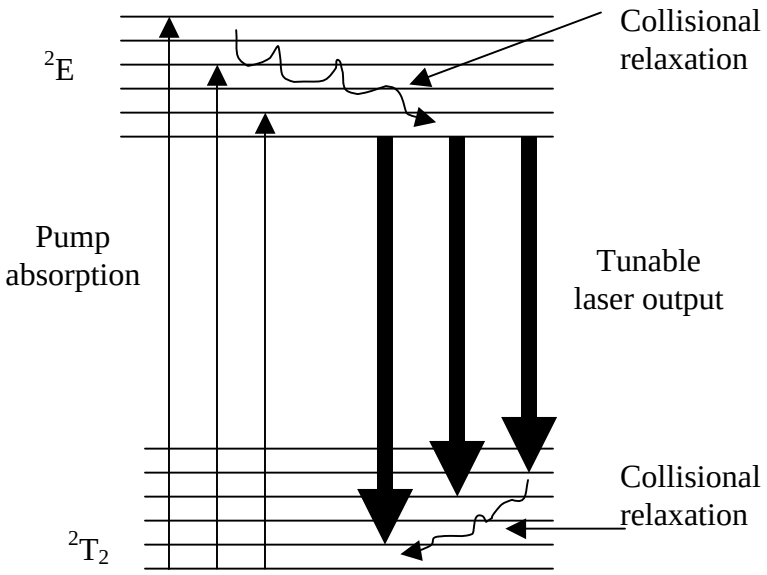

Figure 2.1 Energy levels of the Ti:sapphire laser

conductivity, comparable to metals at low temperature, enables pumping powers as high as 20W from a CW laser. This in turn enhances essential nonlinear optical effects in the crystal and the output power. High optical quality Ti:sapphire crystals are now readily available from commercial vendors in a variety of sizes.

II.1.1 Theory of operation

For a high gain medium like sapphire, it is not difficult to make a CW laser. But it is difficult to build a pulsed laser, especially with an ultra-short pulse width. The Ti:Sapphire laser's success in achieving short pulses width arises from the application of the mode-lock technique.

Any longitudinal mode that satisfies $n\lambda=2L$ (where n is an integer and L is the optical length of the laser cavity.) can oscillate inside the laser cavity. There can be as many as 10^4 longitudinal modes existing in a Ti:Sapphire laser cavity [Ducasse 1998] for a given pulse compared to just a few hundred in a Nd:YAG laser. [Koechner 1996] This is the major reason that ultra-short pulses can be achieved in a Ti:Sapphire laser, since the pulse width in the time domain is inversely proportional to the frequency distribution.

But in a free running laser, those longitudinal modes oscillate simultaneously with a random phase relation between each of them. The resulting laser output intensity is therefore a time-averaged statistical mean value with random fluctuation. If the oscillating modes can be forced into maintaining a fixed phase relationship to each other, the output as a function of time will vary in a well-defined manner. The laser is then said "mode-locked" or "phase-locked". Figure 2.2 illustrates the influence of the phase relation between the modes on the resultant oscillating intensity. With random phase relation, the resultant intensity is like white noise. When the modes are "in phase", a pulse then is formed. As the number of modes involved increases, the pulse also becomes sharper.

There are usually two mode-lock approaches: the active mode-lock technique and the passive mode-lock technique. The former involves the placement of an external modulator while the latter has an absorbing device inside the cavity. However, the mode-lock technique used in the Ti:Sapphire laser is based on a totally different mechanism. [Spence 1991] It utilizes the Kerr-Lens effect. Therefore this type of mode-lock is also known as Kerr-Lens Mode-locking (KLM).

a)

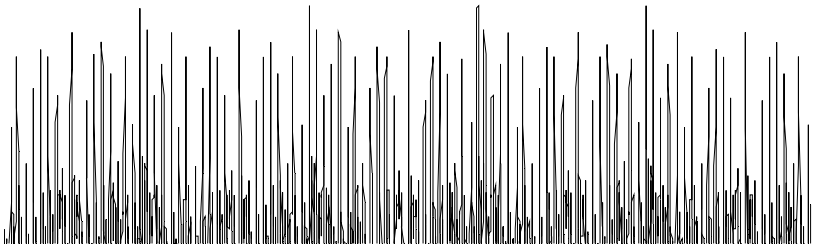

b)

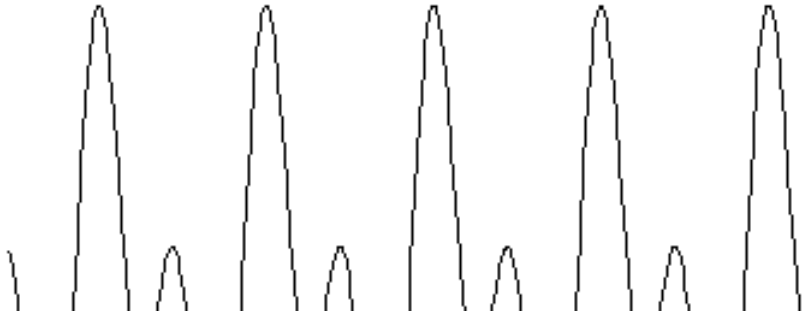

c)

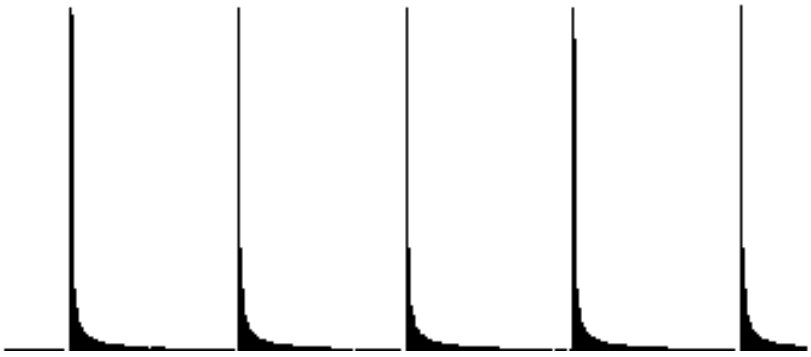

Figure 2.2 Illustration of the influence of the phase relation between the modes on the resultant intensity of the light. a) 100 modes with random phases, b) three modes in phase, c) 100 modes in phase

At sufficiently high intensities, the index of refraction n varies as a function of the beam intensity: $n=n_0+I*n_1$. This is called the optical Kerr effect. Sapphire has a negative n_1. An incident high intensity Gaussian beam can then induce an index of refraction gradient on the crystal. This essentially forms a lens, which self focuses the beam. Therefore an intense beam will have a smaller diameter than a less powerful beam as it traverses the crystal. This self-focusing "lens" is sometimes called a Kerr Lens.

Normally in a laser, there is only one longitudinal lasing mode. This is due to the fact that although the gain medium may have a broad spectrum, it will only emit light at the same frequency as the stimulating light. Hence the earliest light to reach high intensity through the amplification process will establish the frequency for the subsequent emitting light. The resulting emission is essentially in the CW mode. Typically for this mode the beam intensity is relatively low and the beam diameter is then large. If there is an aperture inside the cavity with a diameter less than the beam diameter, there will be loss at this aperture, which further lessons the beam intensity.

To reach mode-lock, there have to be some fluctuations inside the cavity that can generate some high intensity spikes. This can be done by simply tapping a mirror inside the cavity, or more sophisticated in commercial ones, by having a mirror on a Piezoelectiric (PZT) mount and introducing a vibration on the order of a few μm at a frequency of tens of Hz. As the cavity length changes, the lasing longitudinal mode will shift in wavelength. When the change in cavity length is fast enough, the freshly discouraged modes (previously oscillating modes) will die out while new modes begin to lase. This will create a transient period during which more longitudinal modes can exist than under normal circumstances. At some instant if those modes happen to have a fixed phase relationship ("in phase"), a spike with huge peak intensity then is generated. Due to its high peak intensity, the Kerr-Lens effect begins to operate and the beam spot size becomes very small. As a result the beam can pass through the aperture without attenuation. This gain/loss difference obviously favors the mode-lock over the CW and quickly leads to dominance by the former. Since many modes lase simultaneously, there are insufficient atoms in the excited states for a period afterwards. As a result a pulse is formed, which will be amplified. The more modes involved, the quicker the population-inversion is exhausted. This results in a shorter lasing time, which is equivalent to a shorter pulse width.

The aperture in the cavity can be a physical one, which is referred to as “hard aperture”. But the nonlinear crystal itself can also act as an aperture. Sapphire has a Gaussian spatial profile for its gain with the peak at the center. Since the pump intensity is also the highest at the center, a smaller beam will experience higher gain, which is equivalent to loss for beam with bigger spot size. This is amount to a gain aperture, which is called “soft aperture”.

After the pulse is formed, the subsequent stability of the pulse is dependent upon two phenomena. The first is group velocity dispersion (GVD) and the second is self-phase-modulation (SPM).

When a pulse propagates in a medium, its group velocity can varies according to the frequency distribution of the pulse. This is called group velocity dispersion and is defined as:

$$k'' = \left.\frac{\mathrm{d}^2 \mathrm{k}}{\mathrm{d}\omega^2}\right|_{\omega_0} = \frac{\mathrm{d}}{\mathrm{d}\omega}\left(\frac{1}{\mathrm{v_g}(\omega)}\right)_{\omega_0} \qquad \textbf{(2-1)}$$

GVD governs the rate at which the frequency components of a wave packet change their relative phases. As different frequency components travel at different velocities inside the cavity, the fixed phase relationship among them will be lost and this can lead to a broadening of the pulse, or in worse case, even destroy the pulse. This effect can be elegantly shown mathematically as follows.

A Gaussian pulse wave packet can be expressed as

$$E(t) = E_0 \exp(-\Gamma t^2)\exp(i\omega t) \qquad \textbf{(2-2)}$$

As this pulse propagates in a transparent medium, the resulting dispersion can be described by

$$E(x,t) = \sqrt{\frac{\Gamma(x)}{\pi}}\exp\left[i\omega_0\left(t - \frac{x}{V\phi(\omega_0)}\right)\right]\exp\left[-\Gamma(x)\left(t - \frac{x}{Vg(\omega_0)}\right)^2\right] \qquad \textbf{(2-3)}$$

where $v_\Phi(\omega_0) = \left(\frac{\omega}{k}\right)_{\omega_0}$, $v_g(\omega_0) = \left(\frac{\mathrm{d}\omega}{\mathrm{dk}}\right)_{\omega_0}$, $\frac{1}{\Gamma(x)} = \frac{1}{\Gamma} + 2ik''x.$

Rewriting $\Gamma(x)$ as

$$\Gamma(x) = \frac{\Gamma}{1+(2\Gamma k'' x)^2} - \frac{\mathrm{i}(2\Gamma^2 k'' x)}{1+(2\Gamma k'' x)^2} \qquad \textbf{(2-4)}$$

and substituting it into (2-3), the second exponential term on the right side of (2-3) can be written as:

$$exp\left[\frac{i(2\Gamma^2 k'' x)}{1+(2\Gamma k'' x)^2}\left(t-\frac{x}{Vg(\omega_0)}\right)^2\right]exp\left[-\frac{\Gamma}{1+(2\Gamma k'' x)^2}\left(t-\frac{x}{Vg(\omega_0)}\right)^2\right] \qquad \textbf{(2-5)}$$

In the case of GVD, k″ is non-zero. The real part of (2-5) is still a delayed Gaussian function. But its form factor $\frac{\Gamma}{1+(2\Gamma k'' x)^2}$ is always smaller than the original Γ. This results in a broadening of the pulse width. The imaginary part of (2-5) corresponds to a phase modulation with a second order time dependency. A pulse with a time-dependent frequency is called a "chirped" pulse, which, under certain circumstances, will eventually dissolve.

Phase modulation due to interaction between a pulse and some optical element can be written generally as

$$\tilde{E}_{out}(x,t) = \tilde{R}(x,t)\tilde{E}_{in}(x,t) \qquad \textbf{(2-6)}$$

where $\tilde{R}(x,t)$ is the complex modulation function and can be further written as

$$\tilde{R}(x,t) = R_0(x,t)e^{i\Phi(x,t)} \qquad \textbf{(2-7)}$$

where two real functions $R_0(x,t)$ and $\Phi(x,t)$ describe amplitude dependency and phase response, respectively.

If $\Phi(x,t)$ is a linear function of time, there will be at most a shift in central frequency of the pulse while the spectrum is left unchanged. But if higher order dependency of time exists, the spectrum will be altered. This nonlinear effect is referred to as phase modulation. Again the Gaussian representation of a pulse in (2-2) can be used as an example. For simplicity, we assume $\Phi(x,t)=\alpha t^2$ and $R_0(x,t)$=constant.

The modulated pulse can then be written as

$$\tilde{E}_{out}(x,t) = R_0 e^{i\alpha t^2} E_0\, exp\left[-\Gamma\left(t-\frac{x}{V_g(\omega_0)}\right)^2\right]exp\left[i\omega_0\left(t-\frac{x}{V_\Phi(\omega_0)}\right)\right] \qquad \textbf{(2-8)}$$

Its Fourier transform can be calculated easily

$$\tilde{E}_{out}(x,\omega) \propto exp\left[-\frac{i\omega_0 x}{v_\Phi(\omega_0)}\right]exp\left[-\frac{\Gamma x^2}{v_g^2(\omega_0)}\right]exp\left[\frac{\left(i(\omega-\omega_0)+2x\Gamma/v_g(\omega_0)\right)^2}{4(\Gamma-i\alpha)}\right] \qquad \textbf{(2-9a)}$$

$$\propto exp\left[-\frac{(\omega-\omega_0 - 2\alpha x/v_g)^2}{4\Gamma(1+\alpha^2/\Gamma^2)}\right] exp\left[-ik(\omega_0)x\right] exp\left[-\frac{ik'(\omega_0)x(\omega-\omega_0)}{(1+\alpha^2/\Gamma^2)}\right] \times$$
$$exp\left[-\frac{i\alpha(\omega-\omega_0)^2}{4(\Gamma^2+\alpha^2)}\right] exp\left[\frac{ix^2\Gamma^2\alpha}{(\Gamma^2+\alpha^2)v_g^2(\omega_0)}\right] \qquad \textbf{(2-9b)}$$

The first term on the right side of (2-9b) gives the frequency spectrum. There is a shift in central frequency. More interestingly, the spectral width, which is proportional to $\Gamma(1+(\alpha/\Gamma)^2)$, is clearly broadened. Since the pulse width is inversely related to spectral width, this implies a shortening of pulse width. Unfortunately the remaining terms on the right side of (2-9b) show a phase modulation of the frequency spectrum. This indicates the original fixed phase relationship between different frequencies has been broken. In many circumstances, this prevents the shortening of pulse widths and in worse cases, depending on the exact form of $\Phi(x,t)$, even destroys the pulse. In figure 2.3 both a pure Gaussian pulse and one with phase modulation are shown.

The pulse under consideration can be responsible for the nonlinear time dependency of $\Phi(x,t)$. The process then is called self-phase-modulation (SPM). In contrast, if additional pulses cause the phase modulation, it is referred to as corss-phase-modulation. SPM is a big concern in Ti:Sapphire laser due to its effect on pulse formation and stability.

In the time domain, a Gaussian pulse has its intensity peaked at the center. As it propagates in a medium, the index of refraction has a time dependency due to the Kerr effect. This has the effect of having the center of the pulse travelling faster than both the leading and trailing edges of the pulse, thereby altering the pulse shape and causing a phase modulation. For this situation, using the notation in (2-7), the phase factor $\Phi(x,t)$ can be written as $-2\pi n_2 x I(t,x)/\lambda$, where $I(x,t)$ depends nonlinearly on time.

Because self-phase-modulation and group velocity dispersion arise from many optical elements within the laser cavity, some mechanism must be employed to cancel their effect. It is found that in the case of Ti:Sapphire laser, the GVD k″ from lenses and mirrors is positive and the chirp caused by SPM has the same sign (positive) as those arising from GVD. Therefore a natural solution to this problem is to introduce an element inside the cavity with negative group velocity dispersion. It can be shown that a pair of parallel prisms can result in a negative GVD. [Koechner 1996] [Fork 1984] This has become a standard compensation method for the

a)

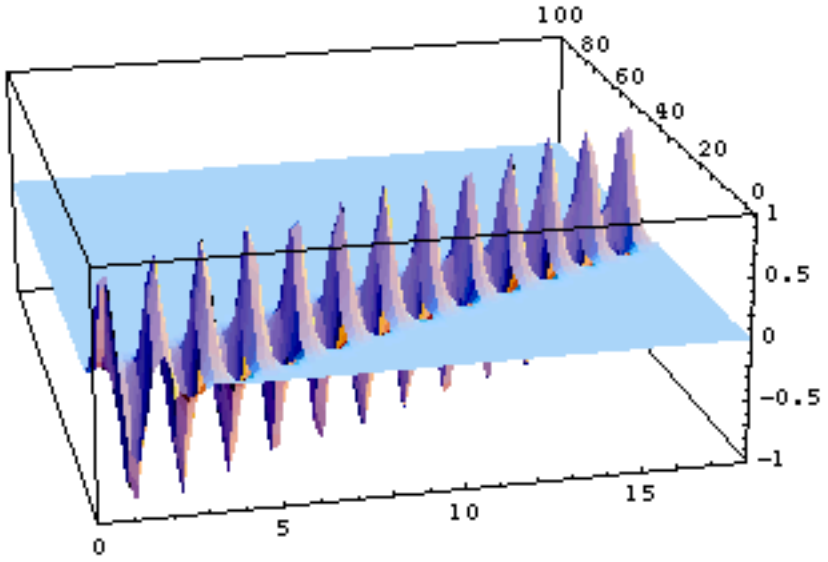

b)

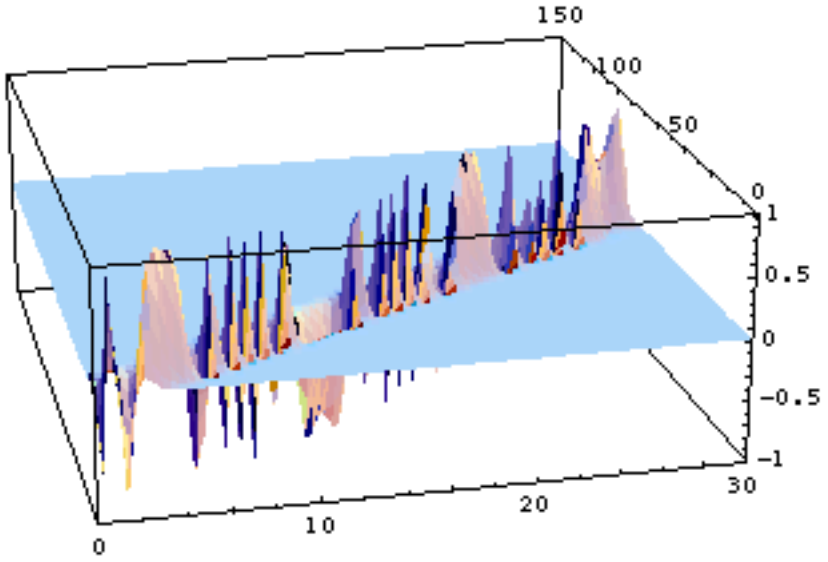

Figure 2.3 Computer simulation of pulse propagation in a media. a) a Guassian pulse; b) a Guassian pulse with phase modulation.

Ti:Sapphire lasers. By adjusting the amount of glass within the cavity, one may fine tune the negative GVD, which may eventually balance the positive chirps.

Because self-phase-modulation and group velocity dispersion arise from many optical elements within the laser cavity, some mechanism must be employed to cancel their effect. It is found that in the case of Ti:Sapphire laser, the GVD k″ from lenses and mirrors is positive and the chirp caused by SPM has the same sign (positive) as those arising from GVD. Therefore a natural solution to this problem is to introduce an element inside the cavity with negative group velocity dispersion. It can be shown that a pair of parallel prisms can result in a negative GVD. [Koechner 1996] [Fork 1984] This has become a standard compensation method for the Ti:Sapphire lasers. By adjusting the amount of glass within the cavity, one may fine tune the negative GVD, which may eventually balance the positive chirps.

The final temporal and spatial form of the pulse is dynamic in nature. Although the prisms and optical materials inside the cavity define the total dispersion, SPM depends on the intensity of the pulse. As the pulse gets shorter, its intensity becomes higher. This leads to more SPM, which can broaden the pulse. As a result of this process an equilibrium pulse is established, which remains unchanged.

II1.2 Alignment and Operation

During the earlier stage of this thesis work, it was necessary to construct a Ti:sapphire laser from basic components. A schematic is shown in figure 2.4. The laser system consists of a focusing lens, a Ti:sapphire crystal, a pair of curved mirrors, a pair of prisms and a pair of end mirrors. An Innova 60 Argon ion laser was used as the pump laser. The focusing lens focused the pump beam onto the crystal. A pair of curved mirrors was to focus the infrared emission through the crystal for amplification. The prisms were used for GVD compensation. The end mirrors forms the cavity with one acting as an output coupler.

The dimensions shown in fig.2.4 have different roles and importance in the operation of the Ti:sapphire laser. The total cavity length L determines the repetition rate f of the pulse as f=2L/c where c is the speed of light in vacuum. The prism separation is somewhat crucial in obtaining the shortest pulse width. The separation between the two curved mirrors and the position of the crystal are very critical. A systematic measurement of the mode-lock stability as a function of the mirror separation and crystal position is shown in figure 2.5. Since the two curved

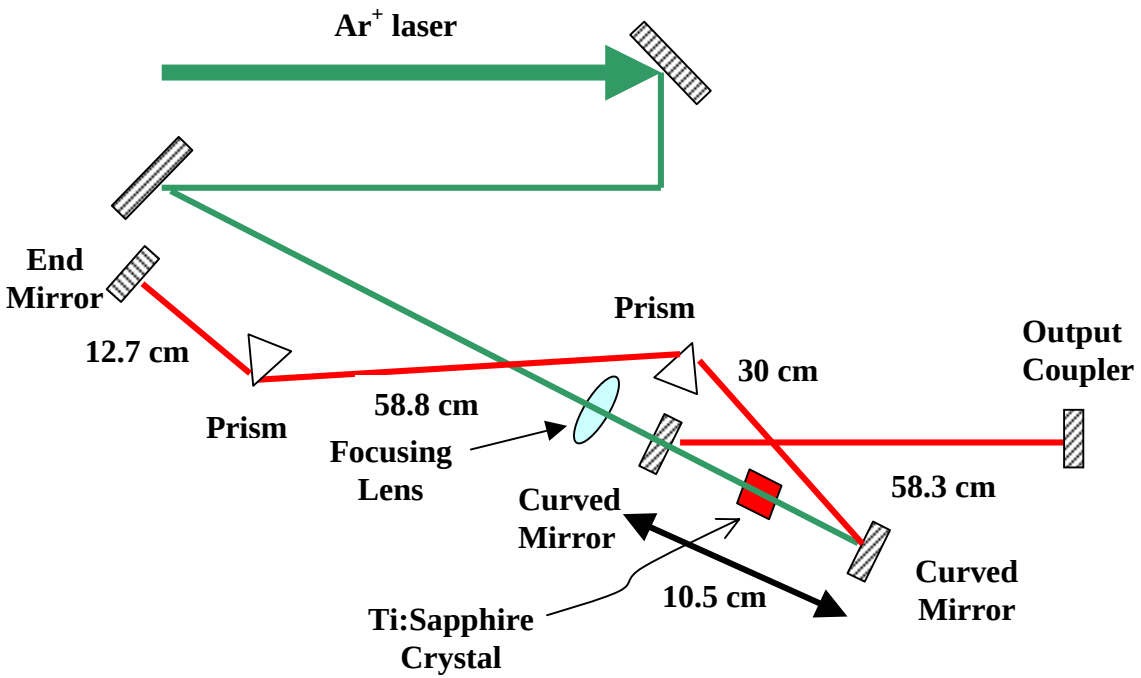

Figure 2.4 Schematic Diagram of a mode locked Ti:Sapphire laser

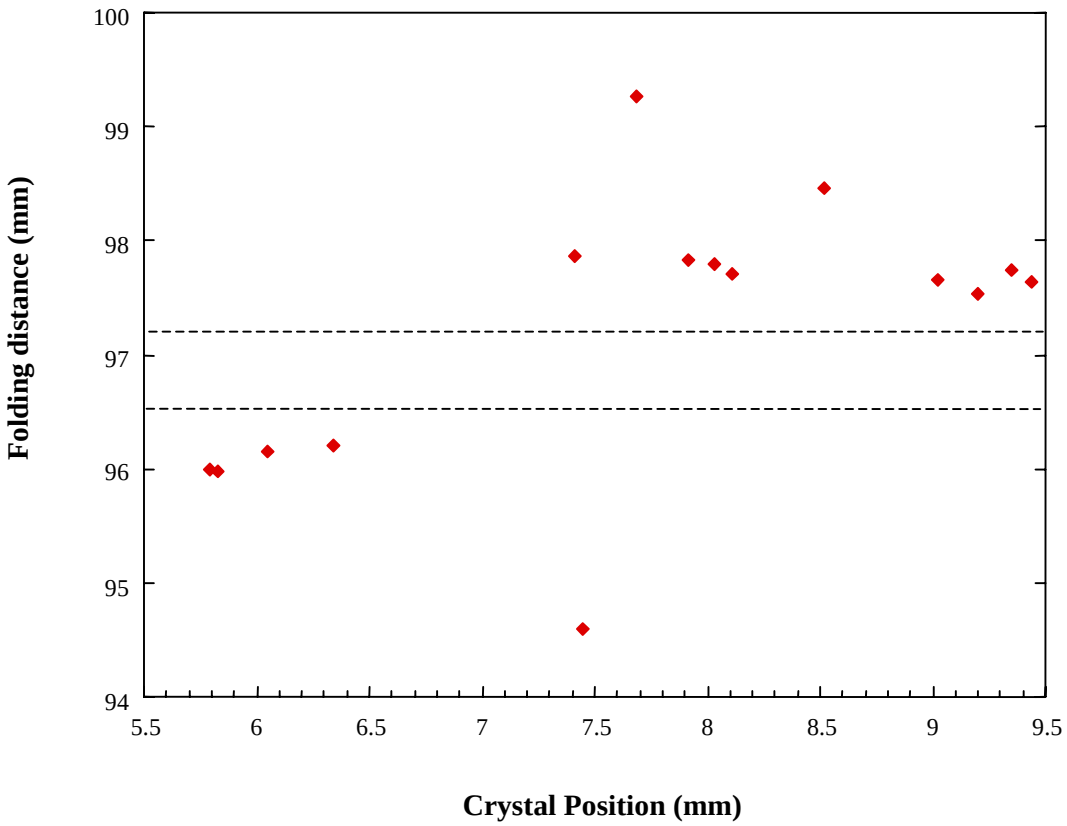

Figure 2.5 Mode-lock stability as a function of folding distance and crystal position. Folding distance=mirror2-mirror1+100 (mm); Crystal position=20-crystal-mirror1. The dots represent stable mode-lock.

mirrors and the sapphire crystal are mounted on separated translation stages, the readings from their micrometers are unrelated. Therefore the separation between the mirrors and crystal positions are the difference between the readings plus an arbitrary offset.

Fig 2.5 shows that a stable mode-lock can be achieved only in two separated areas: one at the bottom left corner and the other at the top right corner. A gap exists between these two areas where no mode-lock can be obtained. This turns out to be consistent with both experimental and theoretical work from other groups. [Cerullo 1994] The gap is predicted from a mathematical model. And Cerullo *et al.* found there are more stable mode-lock configurations in the bottom left corner, which they call low misalignment sensitivity (LMS) region, than in the top right corner, which they call high misalignment sensitivity (HMS) region. [Cerullo 1994] Cerullo explained that the HMS is in an almost confocal configuration, which is sensitive to misalignment, while the LMS is in a configuration with both end mirrors lie in nearly conjugated

planes. Their result is consistent with data shown in Fig. 2.5 as there are more mode-lock points in the upper corner than in the bottom corner.

II.1.3 Characterization of Ti:Sapphire Lasers

The characterization of an ultrafast laser here includes the spectral and temporal descriptions in addition to some other parameters. When the pump laser Innova 60 is running at 5.4 Watts in a multiline mode, the Ti:sapphire laser has a CW power of 400 mW and a mode-lock power of 350 mW. The pulse repetition rate is about 76 MHz.

The frequency spectrum is shown in figure 2.6. It centers at 7824 Å and it has a full width at half maximum (FWHM) of about 230 Å. The dots are the experimental data and the solid line is a Gaussian fit. There is a blip at about 7570 Å, which indicates the existence of CW component in the beam. This component can be filtered out by tuning the prism and the curved mirrors.

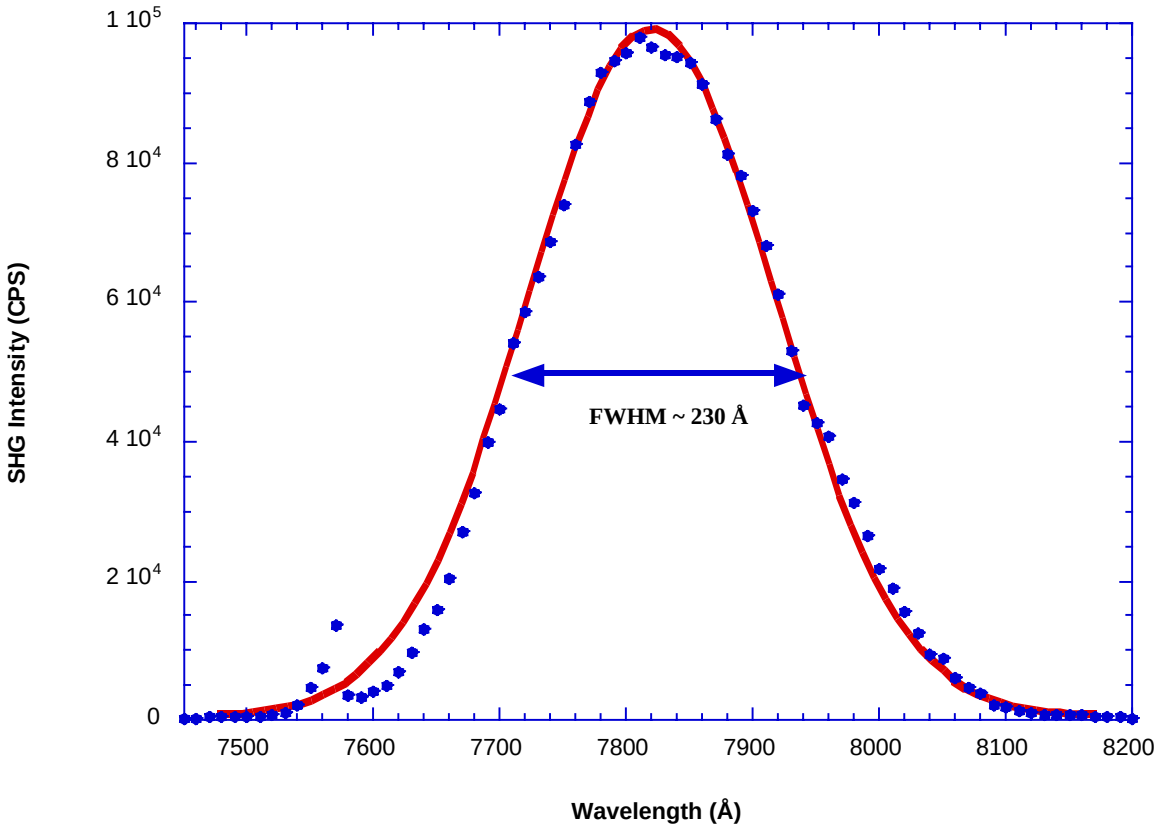

Figure 2.6 Wavelength spectrum of the Ti:sapphire laser constructed at Vanderbilt. The dots are experimental data and the solid line is a Gaussian fit.

To measure the temporal profile of an ultrafast light pulse is obviously a challenge. Although some recent results for recovering pulse envelopes of a few hundreds of femtosenconds directly from electronic devices seems promising, [Sarger 1998] these attempts so far are limited by the materials' response time arising from the photoelectric effect. The alternative is an all-optical method, which gives indirect measurement of pulse widths from tens of picoseconds to considerably less than 100 femtoseconds. But in utilizing this method, one has to not only take into account the technique itself, but also realize that the final pulse shapes are usually model dependent.

The all-optical approach utilizes two different techniques. The first technique makes use of a time-space transformation. It takes only a picosecond for light to travel 300 microns in air, a distance which is easy to measure and calibrate. In comparison a direct measurement of time in the range of picoseconds is much more difficult. The second technique is the use of a mathematical correlation function as described below.

Given a time-dependent function *F(t)*, if we have a reference function *G(t)* already known, we can measure their cross correlation defined as

$$A(t) = \int_{-\infty}^{\infty} F(\tau)G(\tau + t)\mathrm{d}\tau \qquad \textbf{(2-10)}$$

The Fourier transform of (2-10) is

$$\tilde{A}(\omega) = \tilde{F}(\omega)\tilde{G}^{*}(\omega) \qquad \textbf{(2-11)}$$

From equation (2-11) $\tilde{F}(\omega)$ can be readily obtained. An inverse Fourier transform then gives the final answer of *F(t).*

To have higher temporal resolution, it is intuitively clear that the reference function *G(t)* must have a shorter pulse width than the test one. This is equivalent to a broader frequency spectrum for $\tilde{G}^{*}(\omega)$ which enables the calculation of the full spectrum of $\tilde{F}(\omega)$ through (2-11). In the ideal case, the reference pulse should be a delta function and (2-10) yields the exact pulse structure of the signal *F(t)*. But in practice for a pulse width less than 100 fs, it is very hard to find a shorter reference pulse. (Even if one is found, there is still the question of how to calibrate its pulse width.)

The alternative to this is to use the signal *F(t)* itself as the reference and measure the autocorrelation function. An intensity autocorrelation of order (n+1) can be defined as

$$A_n(t) = \int_{-\infty}^{\infty} I(\tau) I^n(\tau + t)\mathrm{d}\tau \qquad \textbf{(2-12)}$$

For a reasonably peaked function *I(t),* as *n* reaches infinity, I^n approaches to a delta function and autocorrelation function $A_n(t)$ becomes a good approximation of the pulse shape *I(t).* Though nonlinear order autocorrelation is very powerful to determine the pulse profile, it usually requires nonlinear optical process. This limits most autocorrelation measurements to the second order. But coupled with spectroscopic measurements, second order autocorrelation can still reveal a large part of the pulse structure.

The first order intensity autocorrelation is defined as

$$A_1(t) = \int_{-\infty}^{\infty} E(\tau) E(\tau + t)\mathrm{d}\tau \qquad \textbf{(2-13)}$$

and is also called second order electric field autocorrelation. The Michelson interferometer is the most common device used for measuring $A_1(t)$. The Fourier transform of (2-13) yields $\left|\tilde{E}(\omega)\right|^2$ which is the spectral intensity of the pulse. Therefore a first order intensity autocorrelation does not carry much more information than that provided by a spectrometer. The Fourier transform results in the absolute value of the spectral intensity. This means the loss of phase information. As a result, an inverse Fourier transform cannot be performed except for the case of Fourier transform limited pulses, in which case the phase is frequency independent.

The second order autocorrelation is usually obtained by measuring the quantity $S_2(t)$ defined as

$$S_2(t) = \int_{-\infty}^{\infty} \left| E(\tau) + E(t + \tau) \right|^4 \mathrm{d}\tau \qquad \textbf{(2-14)}$$

where *E(t)* is the electric field and can be written in general as $E_0(t)\exp[i(\omega t + \phi(t)]$. Equation (2-14) can then be expanded into

$$\begin{aligned} \mathbf{S}_2(\mathbf{t}) = & \int_{-\infty}^{\infty} \left[\left|\mathbf{E}_0(\tau)\right|^4 + \left|\mathbf{E}_0(\mathbf{t}+\tau)\right|^4 + 4\left|\mathbf{E}_0(\tau)\right|^2 \left|\mathbf{E}_0(\tau+\mathbf{t})\right|^2 \right] \mathbf{d}\tau \\ & + \int_{-\infty}^{\infty} \left[4\mathbf{E}_0(\tau)\mathbf{E}_0(\tau+\mathbf{t}) \left(\left|\mathbf{E}_0(\tau)\right|^2 + \left|\mathbf{E}_0(\tau+\mathbf{t})\right|^2 \right) \cos\left(\omega\mathbf{t} + \phi(\tau) - \phi(\tau+\mathbf{t})\right) \right] d\tau \qquad \textbf{(2-15)} \\ & + \int_{-\infty}^{\infty} \left[2\left|\mathbf{E}_0(\tau)\right|^2 \left|\mathbf{E}_0(\tau+\mathbf{t})\right|^2 \cos\left(2\left[\omega\mathbf{t} + \phi(\tau) - \phi(\tau+\mathbf{t})\right]\right) \right] d\tau \end{aligned}$$

In the first term on the right side of (2-15), the first two integrands are signals due solely to the original beam and its delayed counterpart, respectively. They are independent of the delay time and form a background. The third integrand is just the second order intensity autocorrelation. The remaining two integrals in (2-15) contain phase information about the pulse. If these two terms are recorded as well as the others, an interferometric autocorrelation is obtained. It gives more pulse information than an intensity autocorrelation due to the phase information contained in the last two terms in (2-15). The interferometric autocorrelation can be exploited to qualitatively test the absence/presence of phase modulation, quantitatively measure a linear chirp and in combination with the pulse spectrum, determine the pulse shape and phase by a fitting procedure. Although interferometric autocorrelation is superior to the intensity autocorrelation, its signal analysis is more complicated. Since the pulse width is usually the parameter of most concern and the intensity autocorrelation approach is equally good for this purpose, most autocorrelation measurements are intensity autocorrelations. The two interferometric terms in (2-15) can be averaged out by the detection system. The resulting measurement is called “intensity autocorrelation with background” in contrast to the “intensity autocorrelation without background” when the first two integrands in the first integral of (2-15) are filtered out.

The second order intensity autocorrelation defined as

$$A_2(t) = \int_{-\infty}^{\infty} I(\tau) I(\tau + t) \mathrm{d}\tau \qquad \textbf{(2-16)}$$

can be obtained through a second order optical process like second harmonic generation or two photon absorption. The autocorrelator is usually a modified Michelson interferometer. A schematic of one autocorrelator using the second harmonic generation technique is shown in figure 2.7. It differs from a standard Michelson interferometer. It has a nonlinear crystal in front of the detector and the SHG signals from the crystal are recorded by the detector. Since nonlinear optical processes critically depend on excitation beam intensity, a lens is placed in front of the doubling crystal. For an autocorrelator utilizing two-photon absorption, the detection system is different. In place of the doubling crystal and detector, there is only a photodiode with a band gap greater than the photon energy, but less than twice of the photon energy.

A second order intensity autocorrelator was constructed for research carried out for this thesis. It uses second harmonic generation and follows the design shown in fig. 2.7. A 50%

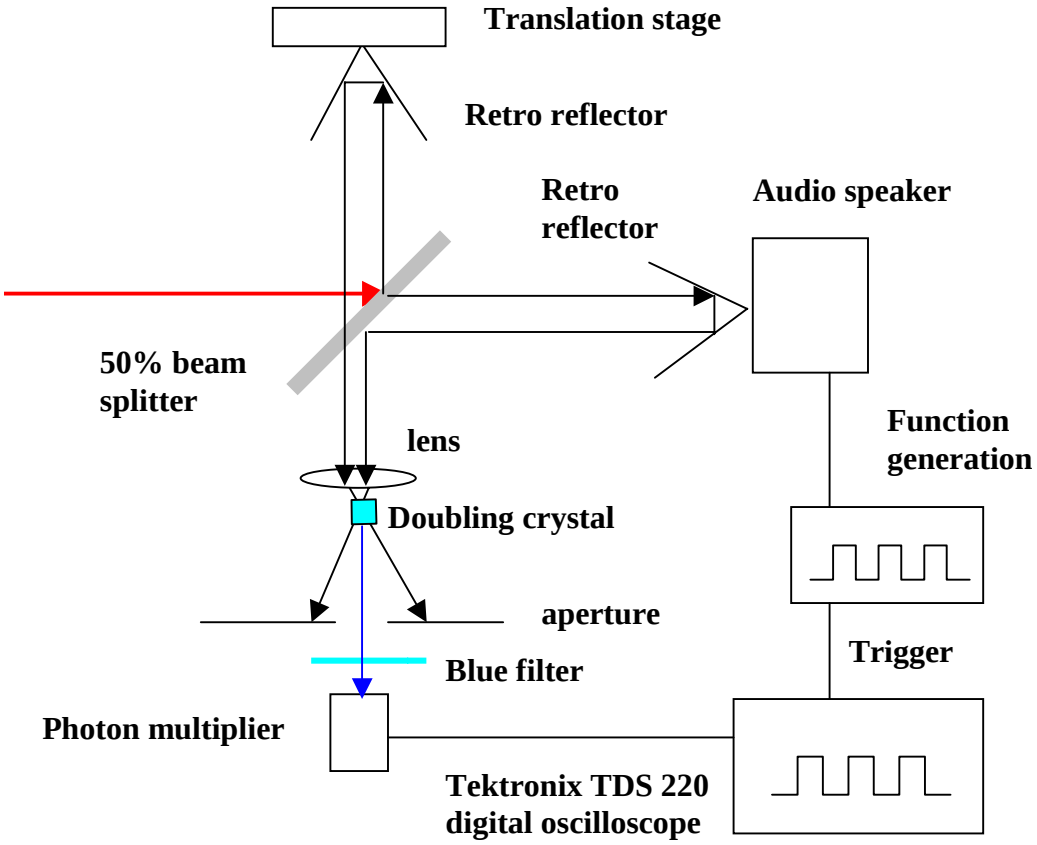

Figure 2.7 Schematics of second order intensity autocorrelator using second-harmonic-generation

quartz beam splitter separates the laser beam into two beams with a time delay t between them. One retro-reflector in the fixed arm of the interferometer sits on a translation stage. This stage is mainly for the purpose of calibration. Another retro-reflector in the varying arm of about equal length is mounted on top of an audio speaker. When the speaker is on, its vibration causes the movement of the second retro-reflector.

This in turn alters the delay time between the two beams. These two beams eventually are incident onto a lens, which focus both beams into a β-BaB_2O_4 (BBO) crystal. The BBO crystal generates strong second harmonic signals. As beams pass through the BBO crystal, both generate their own second harmonic signals, which correspond to the first two integrands in the first integral of (2-15). These SHG signals along with their fundamental beams are blocked by an aperture behind the crystal. Second harmonic signals can also be generated by the two beams together when they are spatially and temporally overlapped. This signal corresponds to the second order intensity autocorrelation. Due to conservation of momentum, $k_{SHG}=k(t)+k(t+\tau)$, the second harmonic generated by those two beams together is along the bisector of the two wave vectors of the fundamental beams. A blue filter is placed in front of a photon multiplier to block scattering fundamental lights. The function generator supplies a triangle wave function at about 40Hz to the audio speaker. It also has a trigger output that is connected to the digital oscilloscope to synchronize its data recording with the oscillation of the delay time.

A raw data recording is shown in Figure 2.8a. The data is shown in real time and its time scale has to be converted. This requires a calibration of the autocorrelator to determine the conversion scale. A movement of the translation stage changes the delay time and this change can be calculated with the knowledge that light travels 0.3 microns in one femtosecond. Since the oscilloscope is synchronized to the function generator, the change in delay time leads to a shift of the dip on the scope screen. By comparing the time shift on the screen with the real delay time, the conversion scale can be determined. For the case of research carried out in this dissertation, a movement of 130 microns in the translation stage resulted in a shift of 1.6 ms of the dip on the screen. Since the beam travels back and forth at the retro-reflector, there has to be a factor of 2 in the consideration. The conversion rate is then 130*2/(1.6*0.3)=542fs/ms.

The autocorrelation trace after conversion is shown in fig2.7b and the dip is also converted into a peak. The full width at half maximum (FWHM) is found to be about 183 fs. Since the figure shows the measurement of the second order intensity autocorrelation as defined

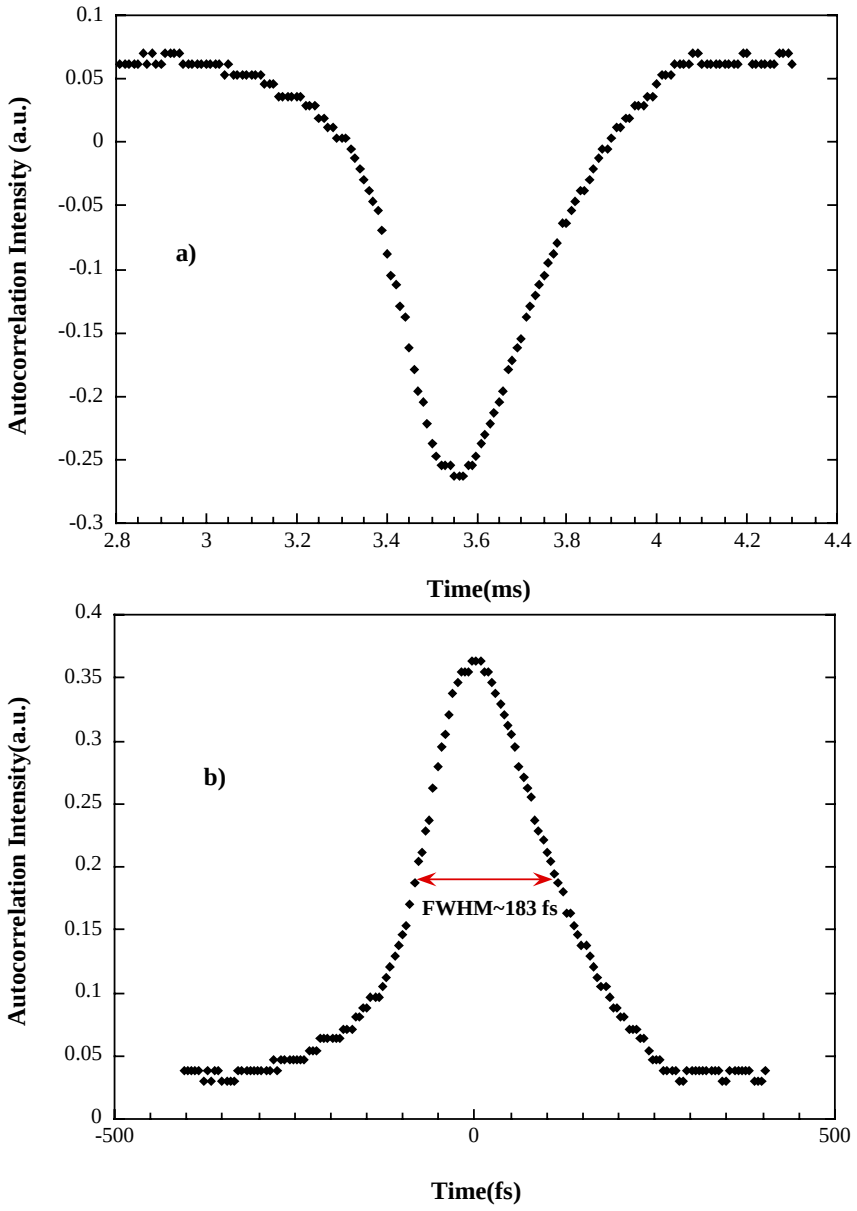

Figure 2.8 An autocorrelation measurement of a home-built Ti-Sapphire laser. a) Raw data; b) scaled data.

in (2-16), the FWHM found is not the same as the pulse width. Since in the second order intensity autocorrelation, the phase information is lost in a Fourier transform, an inverse Fourier transform is impossible except for the Fourier transform limited pulses. As a result, in second order intensity autocorrelation, the most common way to analyze the pulse width is to assume some realistic pulse shape and compute the expected signal from the autocorrelation.

If a Gaussian pulse shape, $E(t)=Exp(-\Gamma t^2)$, is assumed, then the pulse intensity is $I(t)=Exp(-2\Gamma t^2)$ and the pulse width Δt, defined as FWHM of intensity, is $(\ln 2)^{1/2}(2/\Gamma)^{1/2}$. The second order intensity autocorrelation is $Exp(-\Gamma\tau^2)$ with a constant factor. Its width $\Delta\tau$, also defined as FWHM, is $2(\ln 2)^{1/2}(1/\Gamma)^{1/2}$. The ratio between the two pulse widths, $\Delta t/\Delta\tau$, is then $(1/2)^{1/2}$. Therefore from the autocorrelation trace, with certain assumption about the pulse shape, the pulse width can be computed. The ratios for some common pulse shapes are listed in table 2.1. In our case, if the pulse shape is assumed to be Gaussian, the pulse width Δt is about 137 fs.

Pulse spectra in the time domain and in the frequency domain are closely related. A Gaussian pulse can be defined as in (2-2):

$$E(t) = E_0 \exp(-\Gamma t^2)\exp(i\omega t) \qquad \textbf{(2-17)}$$

Its Fourier transform is easily computed as

$$\tilde{E}(\omega) = E_0 \exp\left[-(\omega-\omega_0)^2/4\Gamma\right] \qquad \textbf{(2-18)}$$

The directly measurable quantities are power spectra in both time and frequency domains. If both pulse width and bandwidth are defined as FWHM in respective spectrum, the pulse width Δt in $|E(t)|^2$ is then $(\ln 2)^{1/2}(2/\Gamma)^{1/2}$, while bandwidth $\Delta\omega$ in $|E(\omega)|^2$ is $2(2\Gamma\ln 2)^{1/2}$. Following the convention of using ν, which is $\omega/(2\pi)$, the product of these two, called time-bandwidth product, is a constant equal to $2\ln 2/\pi$. This time-bandwidth product actually applies to all kinds of pulse shapes with of course different constants. Values of this product for some pulse shapes are also listed in table 2.1.

In the discussion so far we have assumed that there is no phase modulation in the pulse. This is a special case and results in Fourier-transform limited or bandwidth limited pulse shapes. In general for phase-modulated pulse, like the one defined in (2-8) and its Fourier transform in (2-9), although the pulse width Δt is still $(\ln 2)^{1/2}(2/\Gamma)^{1/2}$, the bandwidth $\Delta\nu$ is $[2\Gamma(1+\alpha^2/T^2)\ln 2]^{1/2}/\pi$. So the time-bandwidth product is $2\ln 2(1+\alpha^2/T^2)/\pi$. Since $(1+\alpha^2/T^2)$ is always greater than 1, the time-bandwidth product is at its minimum in the Fourier-transform

limited case. The time-bandwidth product is a very important parameter of a pulse shape. It shows the shortest pulse width achievable for a given bandwidth, or for a given pulse width, the minimum bandwidth required.

Table 2.1 Typical pulse shapes, their time-bandwidth products, and intensity autocorrelations.

$E^2(t)$	$\|E(\omega)\|^2$	$\Delta t\Delta\upsilon$	$A_2(\tau)$	$\Delta\tau/\Delta t$
$\mathrm{Exp}(-t^2)$	$\exp(-\omega^2)$	0.441	$\mathrm{Exp}(-\tau^2/2)$	1.414
$\mathrm{Sech}^2(t)$	$\mathrm{Sech}^2(\pi\omega/2)$	0.315	$\frac{3(\tau\cosh\tau-\sinh\tau)}{\sinh^3\tau}$	1.543

As discussed earlier, in both first- and second-order autocorrelation, the Fourier transforms yield only the absolute values. This means a loss of phase information. This is essentially why the temporal pulse shape cannot be derived from the autocorrelation measurements. But with time-bandwidth product, some phase information is recovered. In the Fourier-transform limited case, all the frequency components are in phase and the pulse reaches its minimum width. In all other cases, the pulse widths are broadened due to phase modulation, i.e. frequency components out of phase. Therefore a measurement of the time-bandwidth product of a given pulse reveals how close the pulse is to the Fourier transform limited case. A big deviation from that constant indicates a strong phase modulation existing in the pulse. In this case, with bandwidth in wavelength of 230 Å and pulse width of 137 fs, a time-frequency product of 1.35 is calculated. Compared to the value 0.441 for a Gaussian pulse, this clearly indicates a strong phase modulation in the pulse. This actually can also be observed from the autocorrelation spectrum, for the pulse shape deviates from a Gaussian shape and is asymmetric.

The Ti:sapphire laser has tuning rang from 780 nm to 820 nm. The tunability in this laser

is achieved through the tuning of the prisms. But as indicated earlier, the positions of the prisms have significant effects on the pulse width. Therefore as the wavelength of the Ti:sapphire laser is changed, its pulse width is also affected.

II.1.4 Mira 900 Ti:Sapphire laser

A commercial Ti:Sapphire laser was purchased at a later time and was also used in this experiment. It consists of a Mira 900 Ti:Sapphire laser, pumped by a Verdi diode laser both from Coherent Corporation. This laser has a pulse width of about 100 fs. Its average power is about 600 mW at 800 nm when pumped at about 6 W. Its repetition rate is close to 80 MHz. Its time-bandwidth product is about 0.94.

The design of this commercial ultrashort laser is almost the same as the one constructed here at Vanderbilt. There are however two major improvements over the "home-built" laser. First, unlike the "home-built" laser, which utilizes the nonlinear crystal as a soft aperture, the Miro 900 has a hard aperture inside the cavity. It consists of a tunable slit sitting in front of the output coupler. By adjusting the slit width, mode-lock initiation becomes easier and the mode-lock mode is also more stable.

The second improvement is actually what distinguishes the Miro 900. It uses a birefringent filter for its wavelength selection. When a light beam goes through a birefringent crystal, the ordinary and extraordinary components of the beam usually emerge with a phase difference. This results in a change in the polarization of the beam when these two components recombine. But when the crystal thickness is carefully chosen, a beam with certain wavelength may pass through the crystal with a phase difference in these two components equal to an integer number of π. The polarization of this beam then remains unchanged.

Inside a laser cavity, a birefringent filter situates at Brewster's angle. Any beams with modified polarization after passing through the crystal will suffer losses at the Brewster surface. The beam with certain wavelength qualifying conditions mentioned earlier passes with no change in its polarization. It can then pass through the birefringent filter as if the filter were not present. This leads to a mechanism of wavelength selection.

Tunibility of the wavelength is achieved by rotating the birefringent crystal in its own plane. This changes the angle between the crystal optic axis and the incident plane. Hence the effective principal refractive indices of the crystal also change. As a result, the optical path

length nL through the birefringent filter is different, which means a different wavelength will satisfy the conditions for an unchanged polarization.

With this technique, Mira 900 Ti:Sapphire laser has a tunability ranging from 780 nm to 900 nm. More importantly since the tunability is achieved through the birefringent filter instead of a prism, the pulse width can be maintained the same.

II.2 Experimental Setup

The experimental set-up is a standard SHG set-up. As shown in Figure 2.9, the excitation beam at around 800 nm first passes through a low-pass filter. This filter is to block higher order harmonics from the laser itself. Not shown in the figure is a pair of steering mirrors following the low pass filter. The beam from the laser is horizontally polarized. The sample is placed horizontally on a rotational table. The electric field at the interface of the sample is therefore vertical. To couple the field of the laser with the electric field at the interface of the samples, the polarization of beam has to be rotated by 90°. A pair of 45-degree-angled mirrors facing each other vertically is inserted to do the job. (Figure 2.10) After that a 5 cm focusing lens focuses the beam onto the sample. After the sample, another 5 cm lens is used to collect the second harmonic generation signals. Due to conservation of momentum, the fundamental beam and the SHG signals move in the same direction after the sample. To separate them, a prism is put in the beam path. Behind it a high pass filter is used to further block any scattering fundamental beams. A photon-multiplier-tube (PMT) is used to record the SHG signals. Not shown in the figure are some Al-coated mirrors used to steer SHG signals. These Al-coated mirrors have the property of high reflection at 400 nm while high absorption at 800 nm. In this experiment it is very important that the sample is level. To make sure of this, the sample is mounted on a rotating table and a Helium laser is used for alignment. The reflected Helium laser beam is then projected onto a screen about 1.5 meters away. As the Helium laser shines on the sample, the table will be rotating. If the sample is level, there will be no movement of the image on the screen. Otherwise the table is to be adjusted horizontally until no change of the image on the screen.

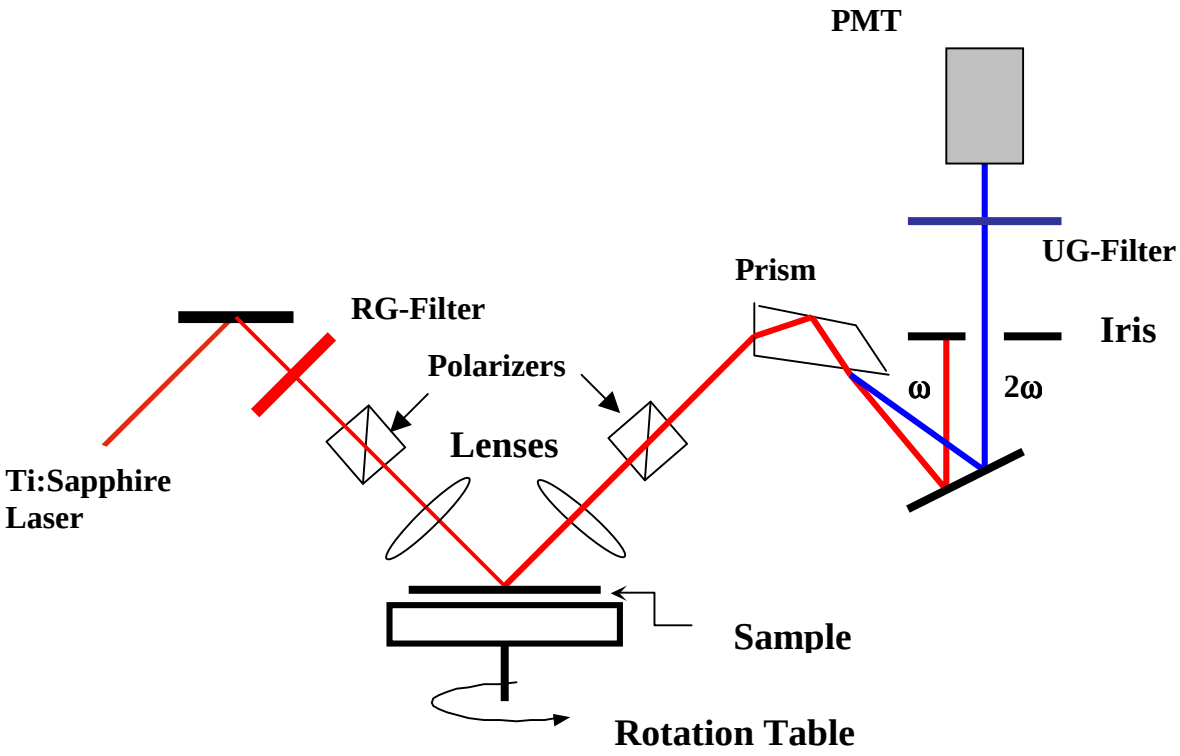

Figure 2.9 Experimental set-up for second-harmonic-generation

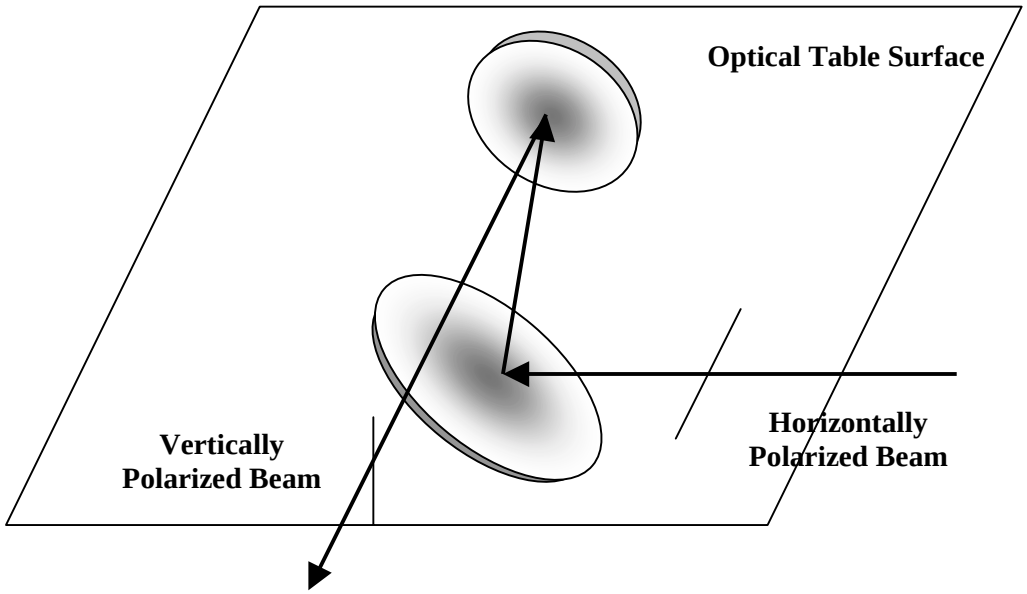

Figure 2.10 Polarization rotator formed by a pair of 45-degree-angled mirrors facing each other vertically.

CHAPTER III

EXPERIMENTAL RESULTS

III.1 Electric Field Induced Second Harmonic Generation (EFISH)

In 1967 Bloembergen *et al.* noticed that second harmonic light generated from silicon and silver showed a significant variation when a dc electric field was applied normal to the surface. [Lee, 1967] This effect later was also detected from other centrosymmetric materials and led to a new field in SHG research, which is called electric field induced second harmonic generation (EFISH). It can be described by:

$$P_i(2\omega) = \chi^{(3)}_{ijk} E_j(\omega) E_k(\omega) E_{dc} \qquad \textbf{(3-1)}$$

where $\chi^{(3)}$ is a third order bulk susceptibility with electric dipole origin. E_{dc} is a quasi-static electric field normal to the surface.

As discussed earlier, in centrosymmetric materials electric dipolar contribution to SHG is forbidden in the bulk. But when an electric field is applied to the bulk, it breaks the inversion symmetry and allows SHG contributions from the bulk electric dipole. Since the bulk susceptibility is third order, this electric-dipole-originated SHG is smaller than the bulk electric dipole contribution from compound materials like GaAs. But when the quasi-static field E_{dc} is sufficiently high, this SHG signal can be comparable to or even higher than that from the surface with dipolar origin and that from the bulk with magnetic dipole and electric quadrupole origins.

Externally applied voltage, as it was in the original work, is the most direct way to generate this quasi-static field. Since most semiconductor devices require an external voltage during their operation, EFISH can be an excellent tool for *in situ* investigation of device performance. Charge trapping or band bending at the interfaces can also build a static field at the interfaces. If this field is strong enough, it can also generate EFISH, which can then provide atomic and electronic information regarding the interfaces.

Several groups have demonstrated the capability of optical SHG for probing static electric fields in crystalline silicon MOS/MS structures, [Dadap 1996] [Lüpke 1995] [Godefroy 1996] Si/electrolyte and Si/SiO_2/electrolyte interfacial regions [Krueger 1993] [Daschbach 1995]

modulated by external voltages. Ohlhoff *et al.* also applied EFISH for monitoring continuous microwave signals on free-running silicon millimeter-wave circuits. [Ohlhoff 1996] Nahata *et al.* conducted time-resolved EFISH measurements of picosecond electrical pulses propagating on a coplanar waveguide transmission line fabricated on silicon. [Nahata 1996] Recent works by van Driel *et al.* show EFISH as a sensitive probe of electron transfer and trapping in the Si/SiO_2 system. [Bloch 1996]

In the theoretical front, Aktsipetrov *et al.* introduced a phenomenological EFISH theory when they were studying EFISH from silicon MOS structure. [Aktsipetrov 1984] [Aktsipetrov 1996] Since the dc electric field varies along the penetration depth of the SHG radiation z_p, a more rigorous expression for the electric-field-induced nonlinear polarization P^{BD} is the form

$$P_i(2\omega) = \chi^{(3)}_{ijk} E_j(\omega) E_k(\omega) \int E_{dc}(z)\,dz \qquad (3\text{-}2)$$

where the integration is taken over the penetration depth z_p.

Aktsipetrov *et al.* however demonstrated that most of the EFISH features, such as the parabolical shape of its bias dependency and the linear dependency of its minimum vs. oxide thickness, can be describe by their model in which electric-field-induced nonlinear polarization P^{BD} is proportional to an electric field $E_{int}=E(z=+0)$ just inside the space charge region (SCR) at the Si/SiO_2 interface. This implies that the real field distribution $E_{dc}(z)$ in the SCR can be replaced by a constant E_{int} inside a layer of effective length z_0 that is comparable to the SCR width. z_0 should be chosen in such a way that $E_{int}\, z_0 = \int E_{dc}(z)\,dz$, where the integration over the SCR satisfies the conservation of charges inside the SCR. This is called interface field approximation, which greatly simplifies the interpretation of EFSIH experiments.

The total second harmonic generation from Si/SiO_2 system can be written as

$$P(2\omega) = \vec{\vec{\chi}}^{BQ} : E(\omega)\nabla E(\omega) + \vec{\vec{\chi}}^{SD} : E(\omega)E(\omega)\delta(0) + \vec{\vec{\chi}}^{BD} : E(\omega)E(\omega)E_{dc} \qquad (3\text{-}3)$$

where the first two terms on the right represent bulk contribution with magnetic dipole/electric quadrupole origins and surface contribution with electric dipole origin, respectively. Both susceptibilities are second order. The last term is the EFISH where the susceptibility is third order.

As mentioned in an earlier chapter, as far as signal detection is concerned, the first two terms in (3-3) cannot be separated. If we define an effective nonlinear susceptibility $\chi^{(2),NL}$ to

describe the two electric field independent SHG contributions, the overall SHG intensity can be written as

$$I^{(2\omega)}(E_{dc}) = \left|\chi^{(2),NL} + \chi^{(3)}E_{dc}\right|^2 I^2(\omega) \qquad \textbf{(3-4)}$$

III.2 Results and Discussion

III.2.1 Sample Preparation and Experimental Method

There are two sets of samples used in the experiment. One set is Si (100) with thermally grown oxide. They were grown at Lucent Technologies. The oxide thickness of the samples varies from 10 Å to about 80 Å. The other set of samples has $ZrSiO_x$ grown on top of Si (100) substrates using remote controlled plasma enhanced chemical vapor deposition (RPECVD). They were grown at North Carolina State University at Raleigh. The thickness is estimated to be several hundreds angstroms.

The experimental set-up was shown in Chapter 2. All the measurements were done in air at room temperature.

III.2.2 SHG from Si/SiO_2 system

Figure 3.1 shows typical second harmonic generation measurements from a Si/SiO_2 system as a function of time. It shows a rapid initial rise and then a gradual increase towards saturation. As equation (3-4) shows, the overall SHG signals consist of two parts: 1. a field-independent contribution from surface dipoles and bulk quadrupoles; and, 2. electric field induced SHG (EFISH). The first contribution is also time independent and contributes a constant background. In the second term, the time-dependent parameter is the static field E_{dc}. Since there is no externally applied electric field at the sample, the dc field in equation (3-4) must be an internal field manifested by band bending at the $Si\text{-}SiO_2$ interface.

Figure 3.2 is the band diagram of $Si\text{-}SiO_2$ system. The barrier for electrons between the silicon valence band and SiO_2 conduction band is about 4.3 eV. The typical photon energy of a Ti:sapphire laser is 1.55 eV (8000 Å in wavelength). This indicates that a three-photon process may possibly inject electrons from Si into silicon dioxide. This injection may then lead to a charge separation, which will create a dc field across the interface. As this static field breaks inversion symmetry in silicon, an EFISH is generated. The time-dependent nature of the electron-injection and field built-up dictates that EFISH is also time-dependent in this case.

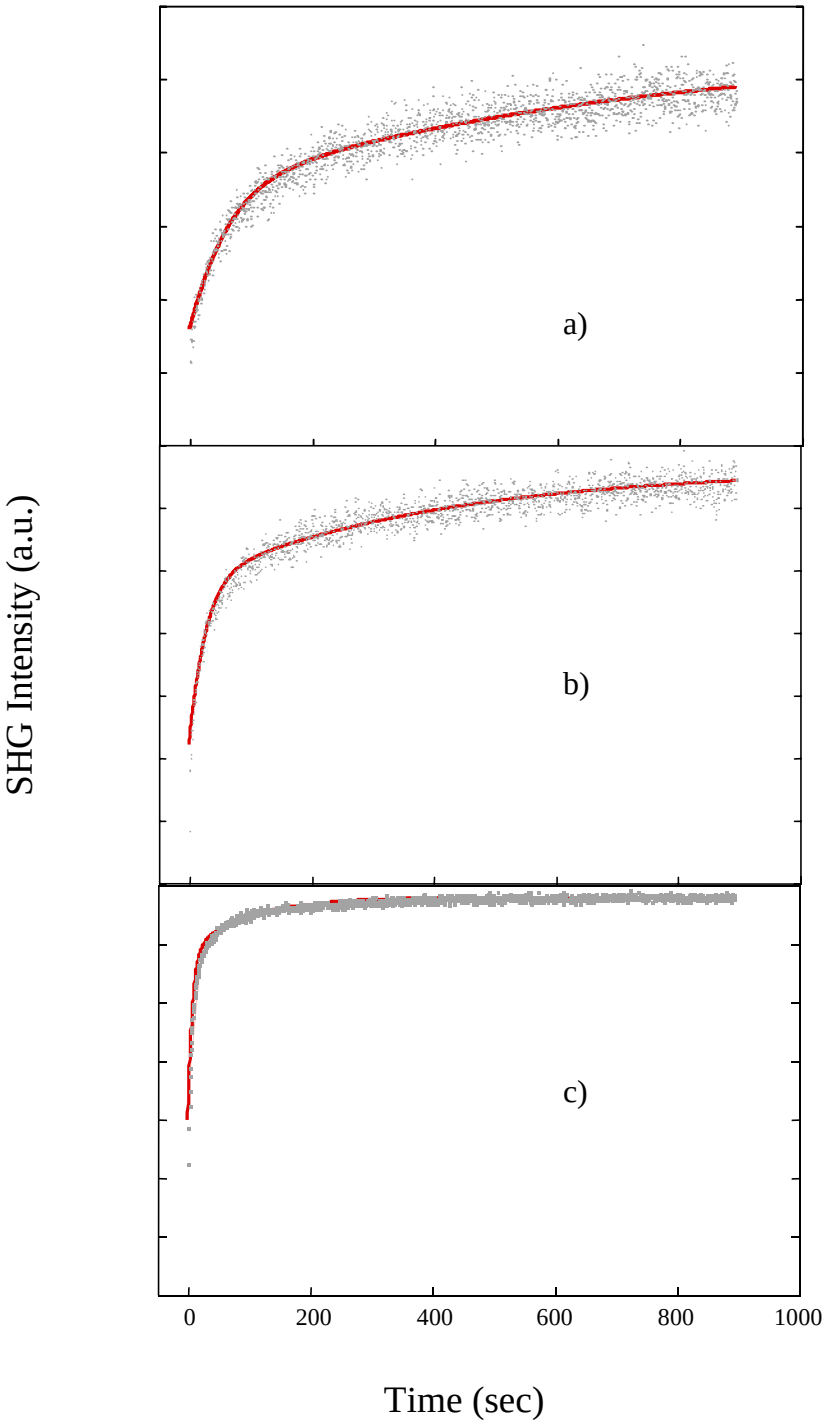

Fig 3.1 SHG from Si-SiO_2 system with a range of intensities. a) 153 mW; b) 269 mW; c) 400 mW. The dots are experimental data and the solid lines are curve fits according to equation (3-14). The photon energy is 1.55 eV.

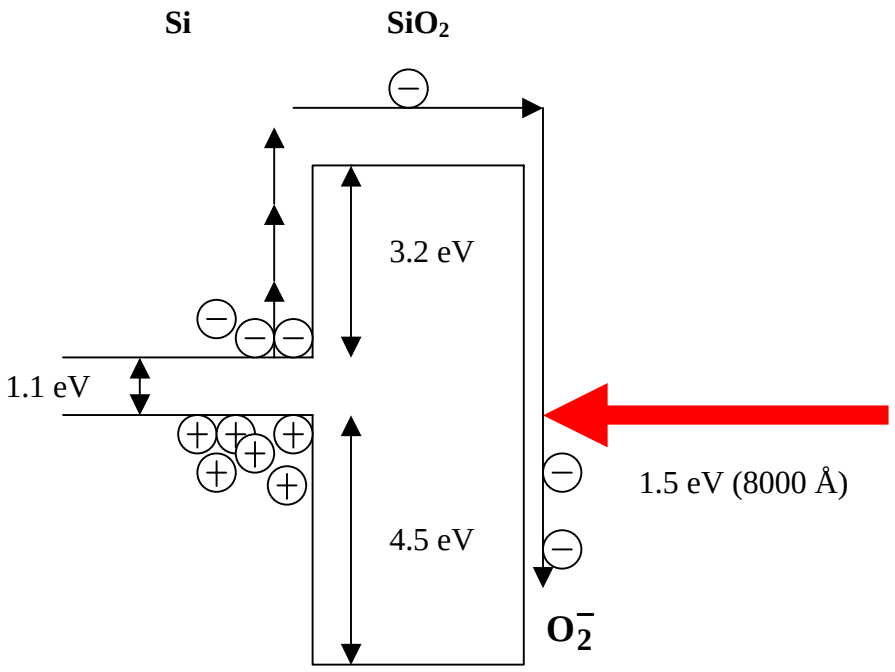

Figure 3.2 Band structure at Si-SiO_2 interface

The experiment by Van Driel has shown some evidence to support the model of three-photon process. [Bloch 1996] In their experiment an Hg lamp was used to pump electrons from silicon into silicon dioxide. A weak Ti:sapphire beam was employed for the sole purpose of generating second harmonic signals at the same time. When photon energy from Hg lamp is greater than 4.38 eV, a SHG feature similar to that in fig 3.1 is observed. This threshold of 4.38 eV, according to Van Driel's interpretation, corresponds to the barrier between the Si valence band and SiO_2 conduction band.

However there are differences between the Hg-lamp-excited SHG experiment and a time-dependent SHG experiment discussed here. In a regular SHG experiment such as the one shown in fig 3.1, due to the high intensity of the Ti:sapphire laser beam, a large amount of electron-hole pairs are created inside the silicon. This populates the conduction band of the silicon and in some cases according to [Sjodin 1998] can even bleach the valence band. Since the conduction band offset at the Si-SiO_2 is about 3.3 eV, a three-photon process between the conduction bands of

silicon and silicon dioxide is also feasible. Van Driel and others recognized this possibility and admitted that they could not distinguish which mechanism works here.

In figure 3.3 the first definite evidence of three-photon process between the conduction bands of silicon and silicon dioxide is shown. As the photon energy decreases to about 1.38 eV (9000 Å), well below the threshold of 1.47 eV for three-photon process between the silicon valence band and oxide conduction band, second harmonic signals still exist. This shows that there must be three-photon electron injection from the conduction band of the silicon into the conduction band of the silicon dioxide.

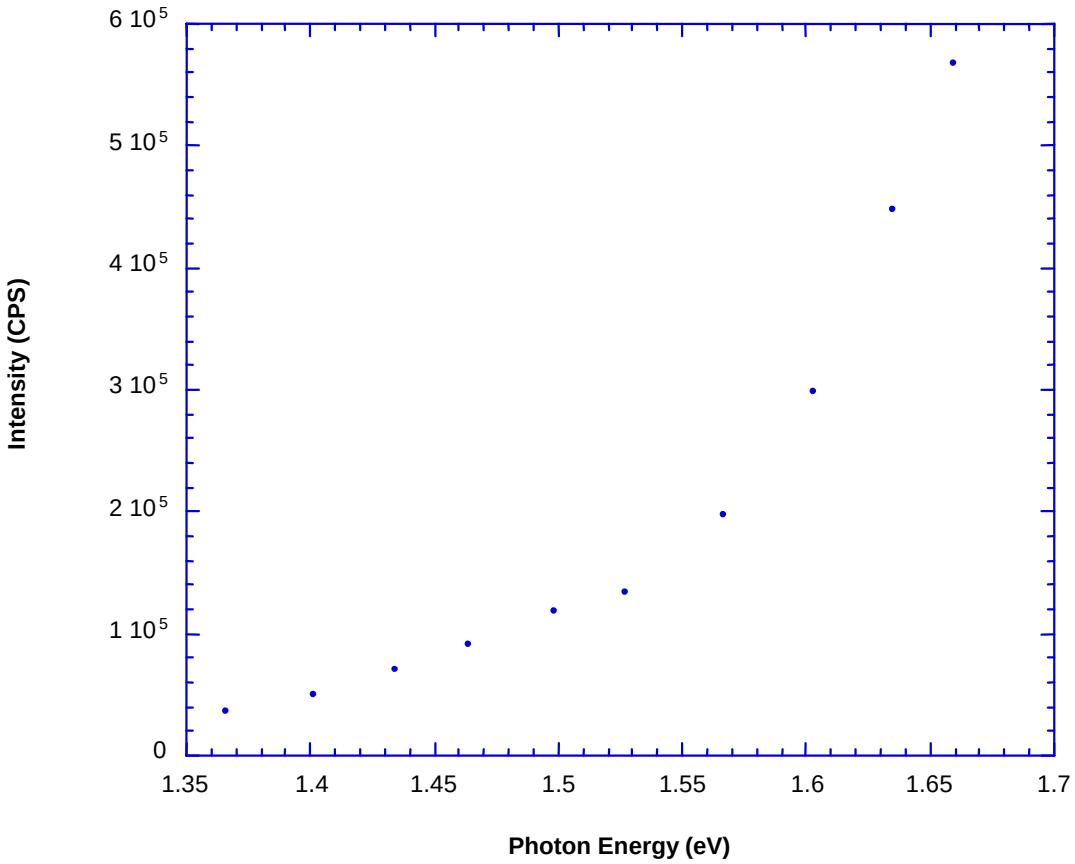

Figure 3.3 SHG from Si-SiO_2 as a function of photon energy

In fig. 3.3, the SHG vs. photon energy curve exhibits a secondary threshold at about 1.55 eV. The SHG signals increase gradually as the photon energy increases from about 1.35 eV to 1.55 eV. Then for photon energy above 1.55 eV, the SHG signals experience a sharp increase. There are two possible reasons for this secondary threshold. First, the threshold energy for three-photon injection from silicon valence band to SiO_2 conduction band is about 1.47 eV. The value of 1.55 eV may be somehow related to this three-photon injection threshold. Second it is well known that in the SHG versus photon energy spectrum of silicon, there is a resonance peak at about 3.4 eV. [Daum 1993] This resonance corresponds to the direct band transition E_1 as shown in Fig 1.2. This resonance also leads to a sharp increase in the SHG signals in the photon energy range above 1.5 eV.

These two effects are intimately related to each other through equation (3-4). Because of the multiphoton injection of electrons, the static field E_{dc} in equation (3-4) will increase as the photon energy increases. On the other hand, due to the direct band transition resonance, the nonlinear susceptibilities, $\chi^{(2)}$ and $\chi^{(3)}$, in equation (3-4) also increase as the photon energy increases. In our experiment, the contributions from these two effects cannot be separated. Further experiments or theoretical models are needed to pin down the origin of this secondary threshold at about 1.55 eV. However the appearance of time-dependent SHG below 1.47 eV in fig 3.3 constitutes definite evidence of three-photon process between the conduction bands of the silicon and the silicon dioxide.

Previous experiments by Pointax [Caplan 1982] and Van Driel [Bloch 1996] have shown that electrons transferred from silicon into the oxide are mostly trapped at the oxide surface. Due to its high electron affinity, oxygen is readily adsorbed on the bare surface of *n*-type semiconductors. [Lunsford 1973] The O_2 molecules can attract and trap electrons from the silicon to form O_2^- at the surface. When light, with photon energy sufficient to inject electron into the oxide, is present, this trapping process is greatly enhanced. Those traps can have lifetimes ranging from seconds to years. Therefore most electrons trapped at those sites will remain during the experiment. Figure 3.4a illustrates this scenario. After a steady state is reached, which means that a large amount of electrons have been transferred to the surface and trapped, the excitation beam is blocked for a few minutes. When the beam is unblocked, the SHG signals immediately return to the steady state level. This shows that the majority of the trapped electrons remain at the surface. In fig 3.4b though, the SHG signals start from the

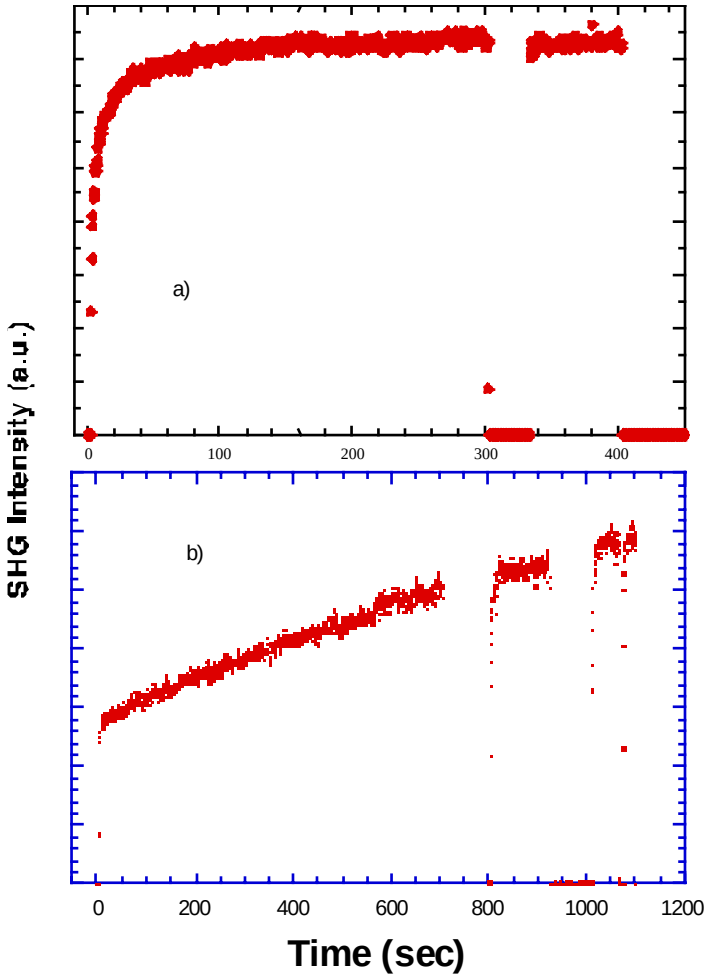

Figure 3.4 SHG from Si-SiO2 with different oxide thickness. a) 40 Å oxide; b) 10 Å oxide.

original level after the excitation beam is blocked for a while. The difference here is the thickness of the oxide. In fig 3.4a, the thickness is about 40 Å while in fig 3.4b it is only 10 Å. As the oxide becomes very thin, the trapped electrons at the surface can easily tunnel back into the silicon. A threshold thickness in the neighborhood of 20-30 Å is inferred. This number is consistent with results from other experiments and theoretical modeling. [Bloch 1996] [Berglund 1971] [Oldham 1986] Another interesting effect in the thin oxide samples is the "memory effect". In Fig. 3.4b, after the beam was blocked and unblocked again, the SHG signal rises at a much faster rate to the previous intensity than it does from a fresh spot. Cernusca suggests that a photo-induced damage process occurs when a fresh spot is irradiated by the laser beam. [Cernusca 1998] The irradiation by the fundamental beams causes multiple effects. 1. The reversible ionization of existing traps through multi-photon injection. 2. The irreversible creation of new traps and their immediate ionization. 3. The generation of second harmonic signals. At a fresh spot, all three processes happen and the increase of the SHG intensity is relatively slow due to the slow process of trap creation. Since the photo-induced damage process is irreversible, for an already-irradiated spot, when the laser beam is on again, the fast ionization process of existing traps dominates and leads to a fast increase in the SHG intensity.

III.2.3 An overview of Si-$ZrSiO_x$ system

Many high-k materials such as Ta_2O_5, and TiO_2, though having dielectric constants as high as 80, are not thermally stable in direct contact with Si. [Wilk 2000] Interface engineering schemes have been developed to form oxynitride and oxide/nitride reaction barriers between the high k materials and Si in an attempt to eliminate or minimize chemical reactions. This increased process complexity for the deposition and control of additional utlrathin dielectric layers, as well as scalability to later technology, poses a great challenge. It is therefore highly desirable to use an advanced gate dielectric, which is stable with Si and has a Si interface quality comparable to SiO_2. $ZrSiO_x$ turns out to be a very promising candidate.

Zirconium silicate, formally expressed as $(ZrO_2)_x$-$(SiO_2)_{1-x}$ ($x<1$), consists of SiO_2 and ZrO_2. There is no bond between Zr and Si atoms. Some important parameters are shown in Table 3.1.

The value of dielectric constant for $(ZrO_2)_x$-$(SiO_2)_{1-x}$ in table 3.1 is from [Blumenthal 1958], in which case $ZrSiO_4$ ($x=0.5$) was measured. It is clear that by adjusting the ratio between

ZrO_2 and SiO_2, the dielectric constant and the band gap of Zirconium silicate can be changed. In the zirconium silicate sample used in this experiment, measurements carried out at North Carolina State University indicate a band gap of about 6 eV. [Wolfe 1999]

Table 3.1 Some important parameters of ZrO_2, SiO_2, and $(ZrO_2)_x$-$(SiO_2)_{1-x}$.

	Dielectric Constant	Band Gap (eV)
ZrO_2	25 [Wilk 2000]	5.1 [Tauber 1971]
SiO_2	3.9	8.9
$(ZrO_2)_x$-$(SiO_2)_{1-x}$	12.6	~6

The stability of Zirconium silicate when it is in direct contact with Si can be best understood through a ternary phase diagram (Figure3.5). The tie lines in the phase diagram

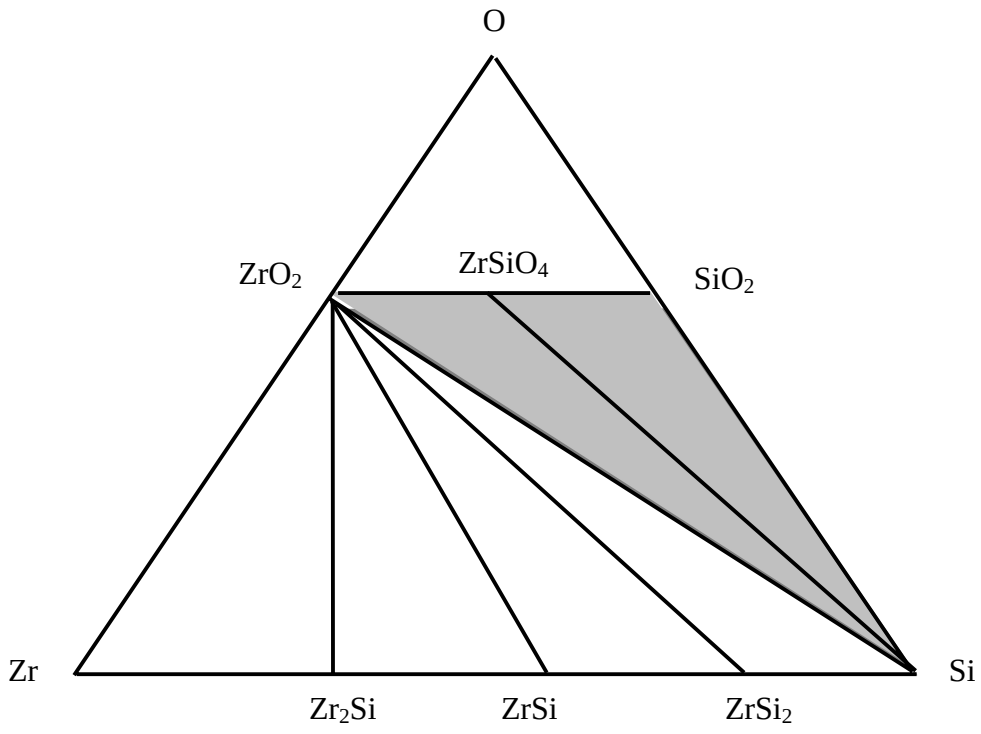

Figure 3.5 Ternary phase diagram for the Zr-Si-O system. After [Wang 1988]

indicate that both ZrO_2 and the compound silicate $ZrSiO_4$ are stable in direct contact with silicon. Actually the shaded area formed by ZrO_2, SiO_2 and Si denotes a large area of $ZrSi_xO_y$ compounds that are expected to be stable in direct contact with silicon. The existence of this large field of stable $ZrSi_xO_y$ compounds shows another potential advantage of zirconium silicate over other insulator materials. Since ZrO_2 has a much higher dielectric constant than that of SiO_2, the level of Zr incorporated into the silicate film can then be gradually increased to meet the demands of technology.

III.2.4 SHG from Si/$ZrSiO_x$ system

Time-dependent SHG measurements for $SiZrO_x$ are shown in figure 3.6. They are strikingly different from those of SiO_2. Although the initial rapid rise is still present, instead of a gradual rise afterwards, a gradual decrease is observed.

As discussed earlier the increase in SHG signal from Si-SiO_2 system has been attributed to the injection, transport and trapping of electrons. The initial rise in SHG from Si-$ZrSiO_x$ has similar features as those from Si-SiO_2. Therefore we hypothesize that in Si-$ZrSiO_x$, the initial rise is also caused by electron injection, transferring and trapping. In addition, we postulate that the more gradual decrease in SHG signals from Si/$SiZrO_x$ system results from the injection, transport and trapping of holes.

As discussed earlier, in Si/SiO_2 system, it requires three photons to inject an electron into the oxide while four photons are needed to inject a hole into the oxide. We hypothesize that this asymmetry in barriers for electrons and holes accounts for the dominant role played by electrons in EFISH measurements in the Si/SiO_2 system with little or no contribution from hole injection. In the Si-$ZrSiO_x$ case, both electrons and holes play an almost equal role in the EFISH measurements. Therefore, it is reasonable to assume that for electrons and holes to play more balanced roles, the barriers for each of them at the Si-$ZrSiO_x$ interface should be more symmetric. Possible carrier dynamics at the Si-$ZrSiO_x$ interface is shown in Figure 3.7. Both electrons and holes are injected into the oxide through multiphoton processes. Since the barriers for both electrons and holes are more symmetric, the band gap of silicon will be near the middle of the band gap of $ZrSiO_x$. The exact values for these barriers are still unknown from the data shown so far and are the subject of experiments discussed later in this thesis. The rate difference between the initial rise and the following decrease is likely due to mobility and trapping cross-

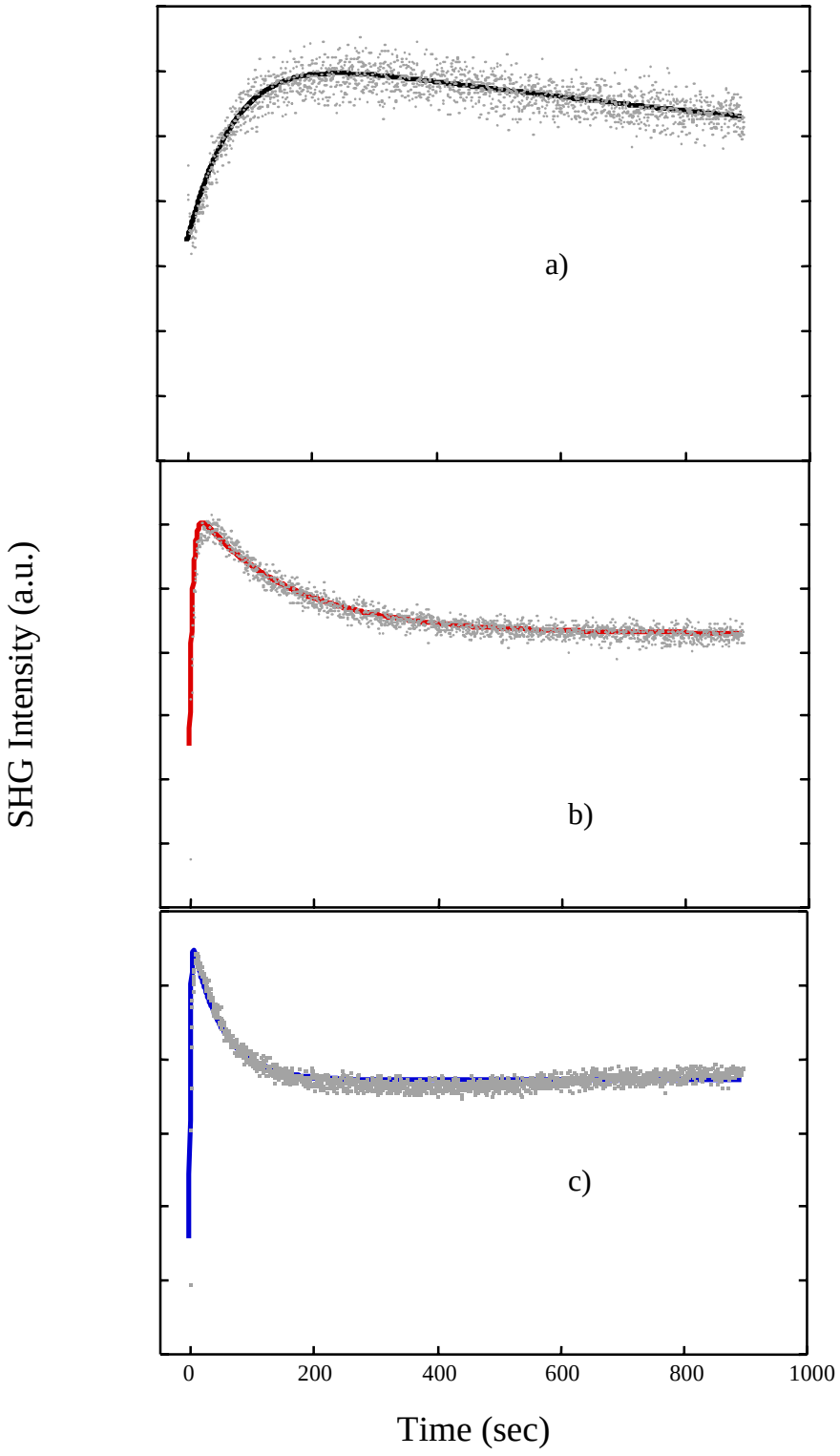

Fig 3.6 SHG from Si-ZrSiOx system with a range of intensities. a) 71 mW; b) 139 mW; c) 222 mW**.** The dots are experimental data and the solid lines are curve fits according to equation (3-15). The photon energy is 1.55 eV.

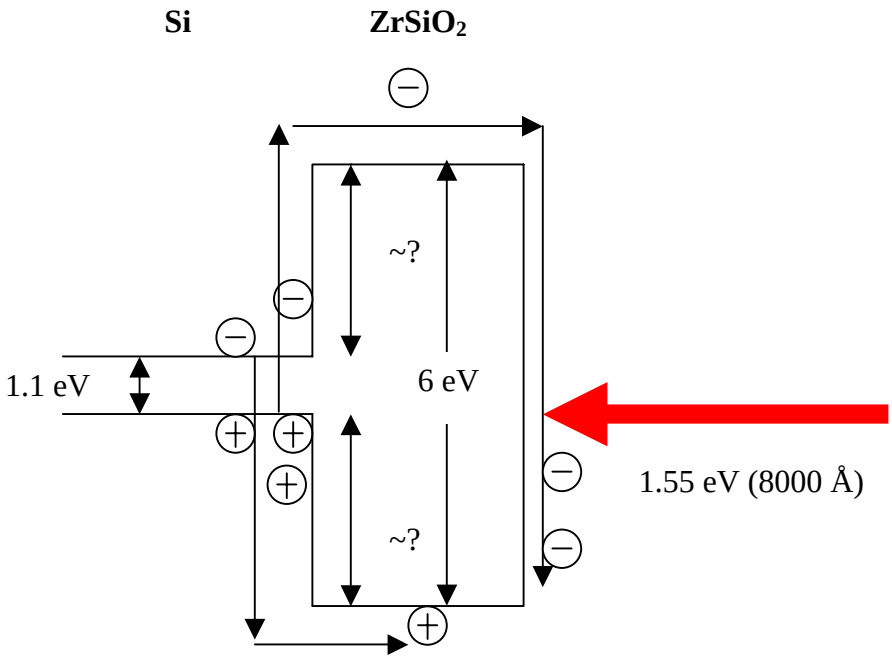

Figure 3.7 Carrier dynamics at Si-$ZrSiO_x$ interface

section differences between the holes and electrons. Although cross-sections for both hole traps and electron traps vary widely in SiO_2, depending on the locations and the types of the electron and hole traps, it is known that electron mobility is several orders of magnitude larger than hole mobility in SiO_2. [Balk 1988] Since ZrO_2 is similar to SiO_2, and the $ZrSiO_x$ sample in our measurements has higher SiO_2 composite than the ZrO_2, it is most likely that electrons in $ZrSiO_x$ will have the same advantages over holes in terms of mobility as they have in SiO_2.

Time-dependent SHG measurements similar to that in fig.3.6 were performed at various photon energies with about the same laser intensities (135 mW). The results are shown in Figure 3.8. There is evidently an abrupt change in the initial rise at photon energy of about 1.4 eV. For photon energy above 1.4 eV, the initial rise is clearly visible. Its magnitude decreases as the photon energy decreases. But when photon energy is below 1.4 eV, the initial rise can no longer be seen.

One possibility regarding the disappearance of the initial rise is that it may be caused by a fast rise, which is beyond the temporal resolution of our measurements. In figure 3.9 the initial rises for various photon energies are shown in the same figure. For those SHG measurements

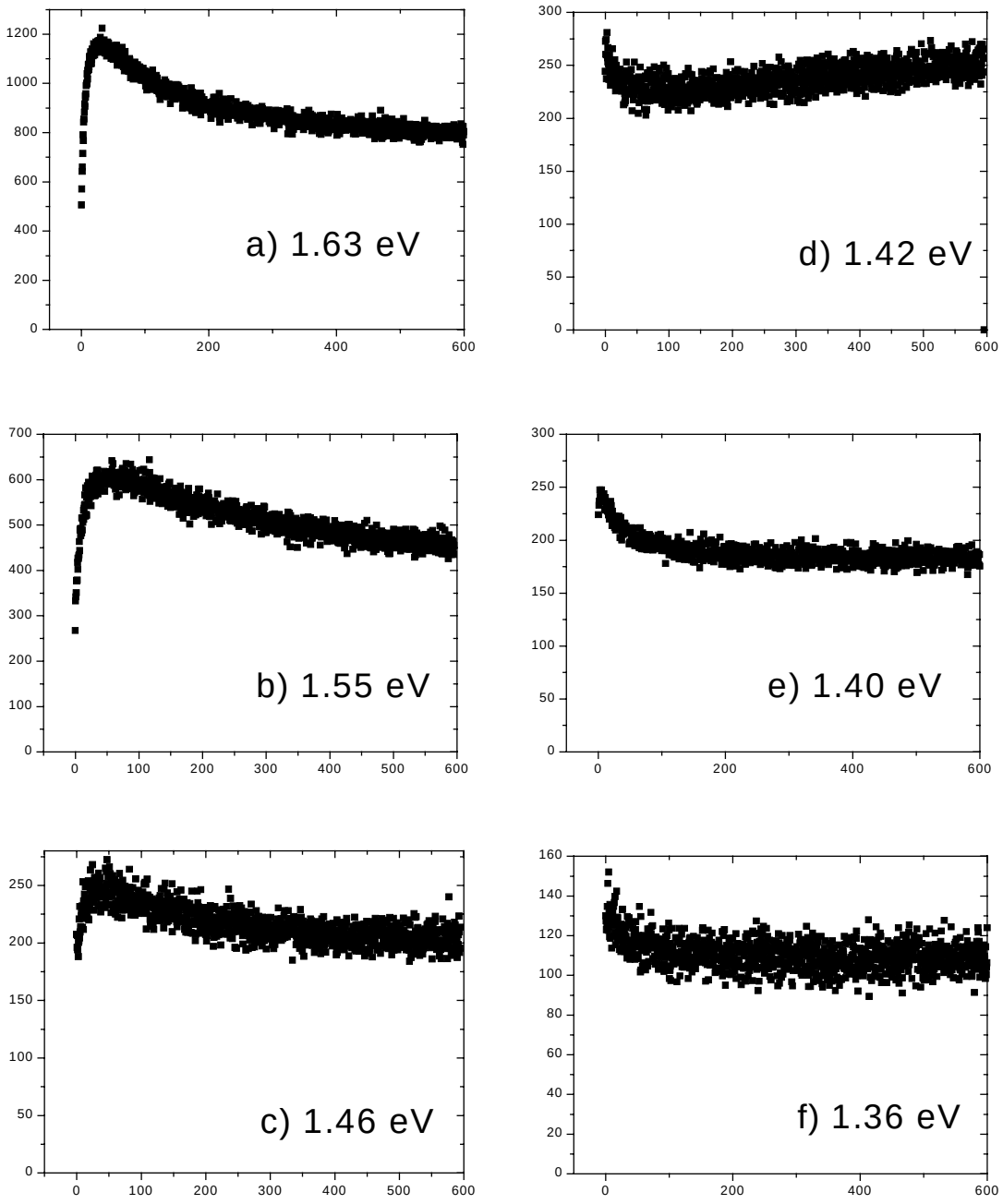

Figure 3.8 SHG signals as a function of excitation photon energy. a. 1.63 eV; b. 1.55 eV; c. 1.46 eV; d. 1.42 eV; e. 1.40 eV; f) 1.36 eV. The Y-axis is SHG intensity in counts/100ms. The X-axis is time in second. The powers are around 135 mW.

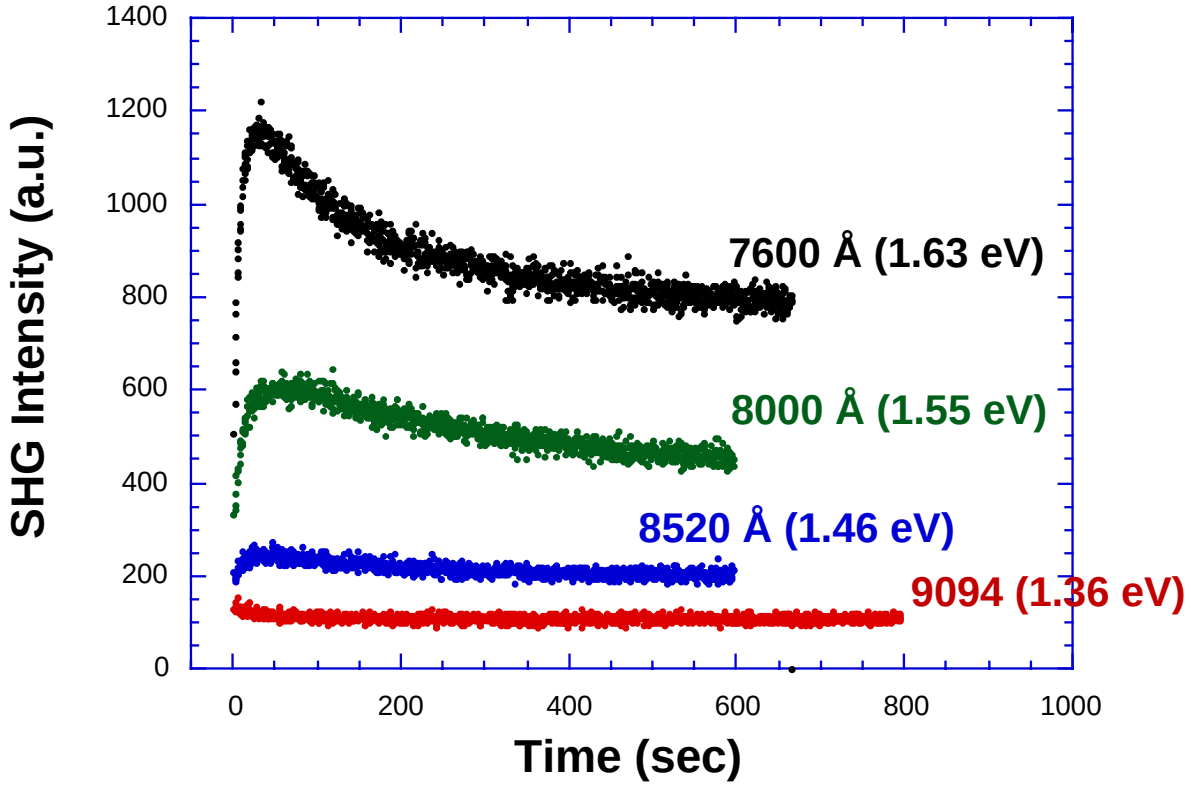

Figure 3.9 SHG from Si-$ZrSiO_x$ with various photon energies.

with photon energy above 1.4 eV, the rate of the initial rise decreases as the photon energy decreases. It is therefore unlikely that for those with photon energies below 1.4 eV, the rate of the initial rise would experience a sudden, huge increase, which goes beyond the temporal resolution of our measurements.

In the light of the data we hypothesize that the observed threshold at about 1.4 eV corresponds to an energy barrier associated with the injection of electrons into the oxide conduction band. Three representative models for band structure at the $Si/ZrSiO_x$ interface are shown in figure 3.10. In the first model (fig. 3.10a), the barrier for electrons injection from the silicon valence band to the oxide conduction band is 2.8 eV. This requires a two-photon process to overcome the barrier with the minimum (threshold) photon energy of 1.4 eV. For photon energies above the threshold, for instance 1.55 eV as shown in the fig 3.10a, the barriers for electrons and holes are obviously asymmetric. Three photons are required for hole injection compared to the 2-photon injection for electrons. In this case electron injection should dominate the EFISH measurements as it does in the Si/SiO_2 system. Since contributions from both electrons and holes are visible in the EFISH measurements from $Si/ZrSiO_x$, the model based on the band diagram in 3.10a can be ruled out.

In the second case (3.10b), the barrier for electron injection measured from the silicon valence band to the oxide conduction band is 4.2 eV. This requires a three-photon process for electron injection with a threshold photon energy at 1.4 eV. Again for photon energy above threshold, the barriers for electrons and holes are asymmetric with holes being favored in this case. Unlike the first case, however, we cannot immediately rule out this model. The carrier dynamics at the interfaces consists of carrier injection, transport and trapping. According to the second model (fig 3.10b), holes (two-photon process) are favored over electrons (three-photon process) in the injection process. But electrons are favored in the transport process due to their larger mobility, while there is no clear favorite in the trapping process due to unknown cross-section difference. The combination of these three processes then may lead to more comparable situations for electrons and holes. Both electrons and holes then can affect the EFISH measurements.

However there are two inconsistencies in the model shown in fig 3.10b. First, according to the model in fig 3.10b, the hole barrier between the silicon conduction band and the oxide valence band is about 2.9 eV. A two-photon process can inject holes across this barrier with a

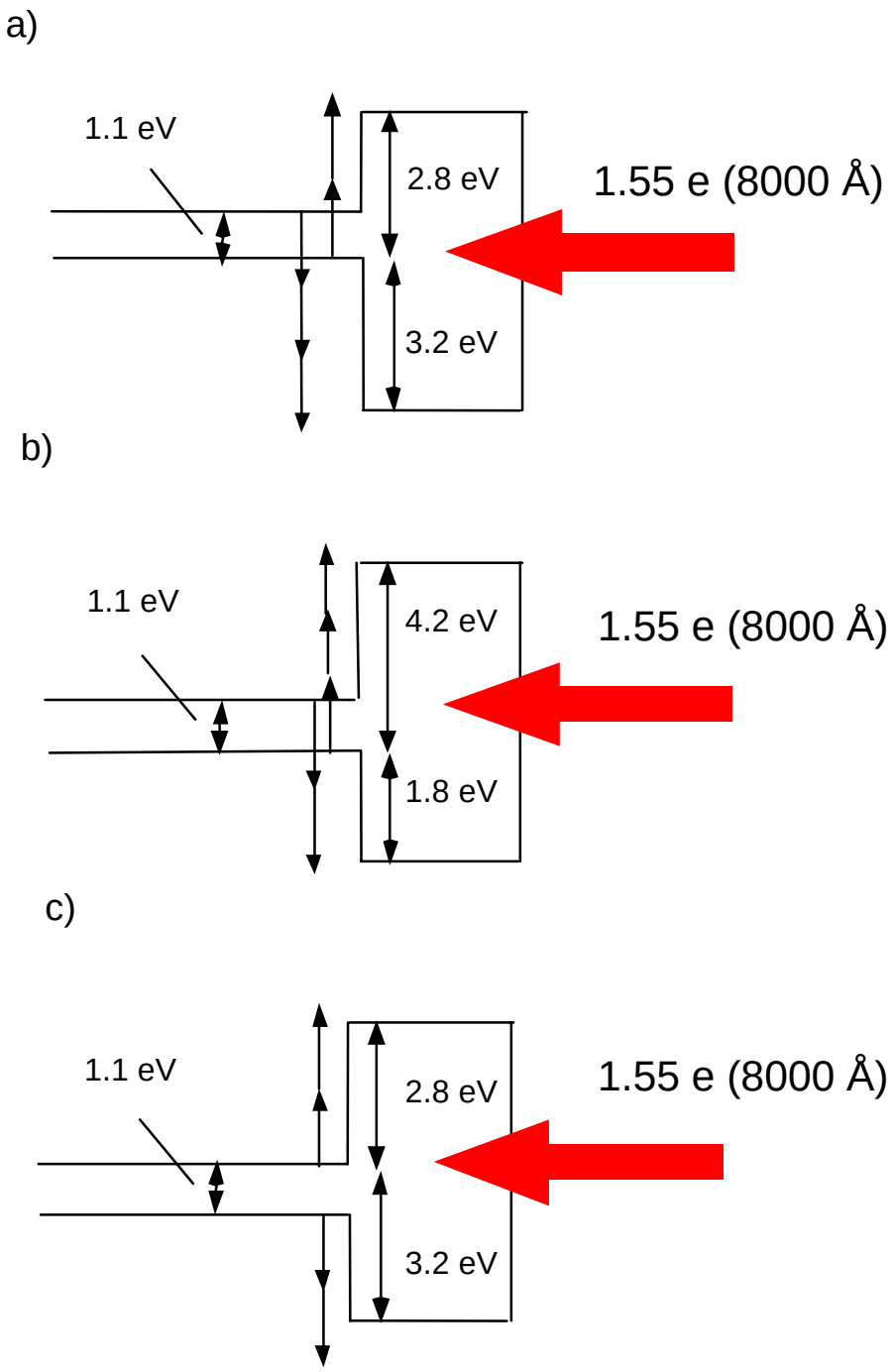

Figure 3.10 Possible band structures at Si/$ZrSiO_x$ interfaces, with 1.4 eV threshold energy corresponding to a) 2-phone injection from valence to conduction band; b) 3-photon injection from valence to conduction band; c) 2-photon injection from conduction to conduction band.

threshold photon energy at about 1.45 eV. But in the wavelength-dependent SHG measurements, there is no abrupt change in the decreasing part of the SHG signals at about 1.45 eV, which would have given signs of threshold for hole injection. Second, the barrier for electron injection from the silicon conduction band to the oxide conduction band is about 3.1 eV according to fig. 3.10b. Electrons can overcome this barrier through a two-photon process with a threshold photon energy at about 1.55 eV. But there is no significant change in the initial rise of SHG signals around 1.55 eV. These inconsistencies suggest that the model shown in fig. 3.10b is questionable.

In the third model (3.10c), the barrier for electron injection from the silicon conduction band to the oxide conduction band is 2.8 eV. A two-photon process is needed for electrons to cross this barrier with a threshold photon energy at or above 1.4 eV. For photon energies above the threshold 1.4 eV, the barriers for electrons and holes are obviously more balanced than the previous two models. Both electrons and holes require two photons to cross the barrier from the silicon conduction band to the oxide conduction band. The holes are slightly favored in injection because of the smaller barrier. This combined with more favored conditions for electrons in transport process can lead to a more balanced roles for electrons and holes in the EFISH measurements. The model in fig. 3.10c shows the most likely band structure at the $Si/ZrSiO_x$ interface.

From equation (3-4), the time-dependent quasi-static field E_{dc} accounts for the SHG variation in time. Systems discussed in this work can be approximated as a parallel plate capacitor with charges with opposite sign on each plate. The electric field generated by this system is then proportional to the charge density on each side of the layer. From Gauss's law, this electric field in silicon at the interface is

$$E_{dc}(z=0) = \frac{\sigma}{\varepsilon_{Si}} \qquad \textbf{(3-5)}$$

The SHG intensity according to equation (3-4) then is

$$I^{(2\omega)}(E_{dc}) = \left|\chi^{(2),NL} + \chi^{(3)}\frac{\sigma(t)}{\varepsilon_{Si}}\right|^2 I^2(\omega) \qquad \textbf{(3-6)}$$

The only time dependent parameter in this expression is the charge density $\sigma(t)$ at the surface.

To determine the charge density $\sigma(t)$, we can write down the rate equation for $\sigma(t)$:

$$\frac{\partial \sigma_n}{\partial t} = \frac{(\sigma_{trap} - \sigma_n)}{\tau_g} - \frac{\sigma_n}{\tau_d} \quad \textbf{(3-7)}$$

where σ_n is the trapped electron density at the surface, σ_{trap} is the total density of electron traps at the surface. τ_g and τ_g are time constants for the electron generation process and dissipation process, respectively.

The time-dependent trapped charge density at the surface is then

$$\sigma_n = A \exp\left[-\frac{t}{\tau_n}\right] + B \quad \textbf{(3-8)}$$

with

$$A = -B = -\frac{\tau_d \sigma_{trap}}{\tau_g + \tau_d} \quad \textbf{(3-9)}$$

$$\frac{1}{\tau_n} = \frac{1}{\tau_g} + \frac{1}{\tau_d} \quad \textbf{(3-10)}$$

The time-dependent SHG intensity can then be written as

$$\begin{aligned} \mathbf{I^{(2\omega)}(t)} &= \left| \chi^{(2),NL} + \chi^{(3)} \frac{\mathbf{eA}\exp\left[-\frac{\mathbf{t}}{\tau_n}\right] + \mathbf{B}}{\varepsilon_{Si}} \right|^2 \mathbf{I^2(\omega)} \\ &= \left| C + \chi^{(eff)} \exp\left[-\frac{\mathbf{t}}{\tau_n}\right] \right|^2 \mathbf{I^2(\omega)} \end{aligned} \quad \textbf{(3-11)}$$

If equation (3-11) is used to fit the time-dependent SHG measurements, the trapping time τ_n can then be extracted. τ_n is a measurement of the time scale for the electron injection, transport and trapping. Its inverse, $1/\tau_n$, is the rate of electron injection, transferring and trapping. This rate should be proportional to the product of the probabilities of all these three processes.

$$1/\tau_n \propto W_{inj} * W_{trans} * W_{trapping} \quad \textbf{(3-12)}$$

The electron injection is a multiphoton process and its probability should then be related to the intensity I of the excitation source through $W_{inj} \propto I^n$, where n is the number of photon involved. Since neither the transferring nor the trapping probability depends on the beam intensity, the overall trapping rate $1/\tau_n$ will then be related to I:

$$1/\tau_n \propto I^n \quad \textbf{(3-13)}$$

If time-dependent SHG measurements are performed for different powers, the trapping rates at these powers can be extracted through the fitting equation (3-11). If these rates are plotted versus the powers, the number n can be extracted, which is the number of photons required for electron and hole injection independently. This will of course give information about the barrier heights for multiphoton injection.

When equation (3-11) is applied to our experimental data, some modifications have to be made. For Si-SiO_2 system, it is clear that a single exponential term does not fit the data well. It is well known there are at least two types of electron traps existing in the Si-SiO_2 system. [Svensson 1988] [Shamir 2000] They are called slow and fast traps, respectively. Using a two-trap model, the SHG intensity can be expressed as

$$I^{(2\omega)}(t) \propto \left| a - b_f \exp\left[-\frac{t}{\tau_f} \right] - b_s \exp\left[-\frac{t}{\tau_s} \right] \right|^2 \qquad \textbf{(3-14)}$$

with *f* and *s* associated with fast and slow traps, respectively.

Equation (3-14) is used to fit the SHG experimental data from Si-SiO_2 system in fig 3.1. The fits are reasonably good which is an indication of the validity of our model. As the excitation beam power is varied, the trapping rate $1/\tau_s$ and $1/\tau_s$ also change. Figure 3.11a shows the trapping rate dependency on the average excitation power. The values for n are found to be 2.3 and 2.6 for fast and slow traps, respectively. This result is close to those from other groups. [Mihaychuk 1995] It is believed that these results are evidence for a three-photon excitation process, with some two-photon contributions arising from the silicon conduction band to the oxide conduction band transitions.

In $SiZr_xO_y$ system, we present evidence that both electrons and holes are injected into the oxide with comparable probability. The charge density σ in equation (3-6) therefore has to be the difference between trapped electron density and trapped hole density in the oxide. We assume that the slow-trap contribution is a higher order term, which we will ignore in this analysis. The time-dependent SHG intensity from Si-$SiZrO_x$ system then will be

$$I^{(2\omega)}(t) \propto \left| a - b_e \exp\left[-\frac{t}{\tau_e} \right] + b_h \exp\left[-\frac{t}{\tau_h} \right] \right|^2 \qquad \textbf{(3-15)}$$

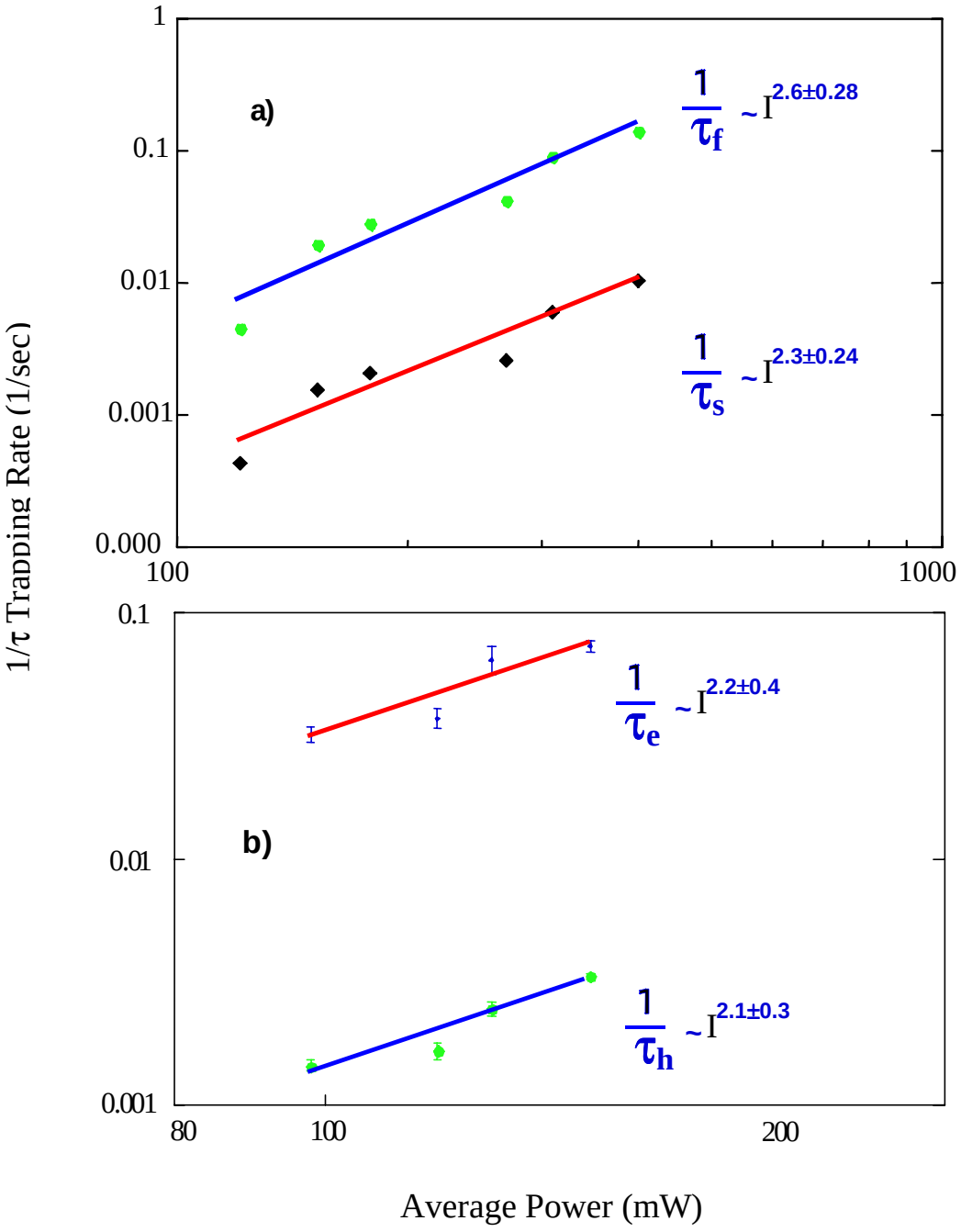

Figure 3.11 Trapping rate dependency on average power. a) Si-SiO_2 system; b) Si-$ZrSiO_x$ system.

Representative fits using equation (3-15) are shown in Fig. 3.6. A typical plot of power dependency on trapping rate is shown in Figure 3.11b. Averaging the values of n from several plots gives us the values of n for electrons and holes as 2.37±0.37 and 2.27±0.22, respectively.

The comparable values of n for electrons and holes in $ZrSiO_x$ indicate that both electrons and holes require a comparable number of photons for injection. Therefore the energy barriers for these two carriers should be close. This is consistent with the model shown in fig 3.10c. The values of n from fig. 3.11b, within uncertainty, are indications of primarily two-photon injection for electrons and holes with perhaps some contribution from three-photon processes. For photon energies higher than the threshold 1.4 eV, according to the model in fig. 3.10c, electrons in the silicon valence band and conduction band need three photons and two photons, respectively, to be injected into the oxide conduction band. The holes in the silicon conduction band and valence band also require three photons and two photons, respectively, to cross into the oxide valence band. Therefore the power-dependent measurements indicate carrier dynamics consistent with the model in fig 3.10c, which suggests primary two-photon processes for both electrons and holes in the EFISH measurements with some contributions from three-photon processes.

The time-dependent SHG measurements at various powers and the consequent curve fittings using equation (3-15) were also performed at other photon energies. For photon energies above the threshold for electron injection at 1.4 eV, the results are consistent with the model shown in fig. 3.10c within experimental uncertainty. But equation (3-15) does not give satisfactory fits for photon energies at or below the photon threshold energy, 1.4 eV.

As the photon energy approaches the threshold for electron injection, there will be little or no electrons crossing the barrier into the oxide. Consequently the component from electron contribution in the fitting equation (3-15) is no longer physically applicable. Hole injection still exists although with diminished magnitude. EFISH due to carrier injection then becomes much smaller. Meanwhile as discussed earlier, besides EFISH caused by carrier injection, there are other non-time-dependent contributions to SHG as shown by equation (3-6). It is known that the most common defect structures in ZrO_2 are doubly ionized oxygen vacancies and singly ionized oxygen interstitials. [Kumar 1972] These defects can attract electrons during their formation in the growth process. A dipole layer then can be formed with electrons in the oxide and positive image charges in the silicon. This results in a in-built electric field across the interface. This field can generate second harmonic signals, which are time-independent. The decreasing SHG signals

shown in fig. 3.8 for photon energy at or below 1.4 eV, which we attribute to hole injection, confirms the existence of this field and its effect on the SHG measurements. (Without the existence of this in-built field, EFISH signals below the threshold 1.4 eV would also have increased in time.) Time-independent SHG signals can also originate from the bulk due to electric quadrupole terms, and from interfaces due to broken symmetry. All these time-independent contributions are small compared to the EFISH signals arising from carrier injection when the photon energy is above the threshold for electron injection at 1.4 eV. These time-independent background contributions have a relatively large effect for photon energies go below 1.4 eV. Therefore, at the low photon energy range (<1.4 eV), EFISH signals due to carrier (hole) injection becomes much smaller than the background SHG signals from other sources. With the low ratio between EFISH signals from hole injection and background SHG signals, equation (3-15) with exclusively hole contribution gives very large uncertainty in fitting the experimental data. Taking these into account, equation (3-15) is not applicable for measurements with photon energies at or below 1.4 eV.

The values for both band offsets shown in fig 3.10c indicate that barriers for both electrons and holes are reasonably large, well above the minimum 1 eV required by many calculations. [Feldman 1998] Hot electrons or holes cannot easily tunnel through the oxide. This gives strong supports to $ZrSiO_x$ as a gate oxide candidate in future generation semiconductor devices.

III.2.5 Thermal effect in SHG from Si/$ZrSiO_x$ system

The similarity in the values of n for SiO_2 and $ZrSiO_x$ is an indication that they have similar origins. Both are electronic in nature instead of thermal. When a laser is used, thermal effects always have to be considered. Measurements for SHG at higher power are shown in figure 3.12. Compared to those at lower power, a third process has appeared which leads to a gradual, but significant, increase in SHG. At very high power this process totally dominates other processes, which have electronic origins (fig 3.12a). At 500-mW power, a measurement of the temperature at the backside of the sample shows an increase of 30° C in less than 1 minute.

To eliminate this effect, the sample is mounted on a large aluminum block, which acts as a heat sink. Measurements were then repeated and compared to those without the heat sink. (fig3.12). The significant increase in SHG signals observed when there is no heat sink has been

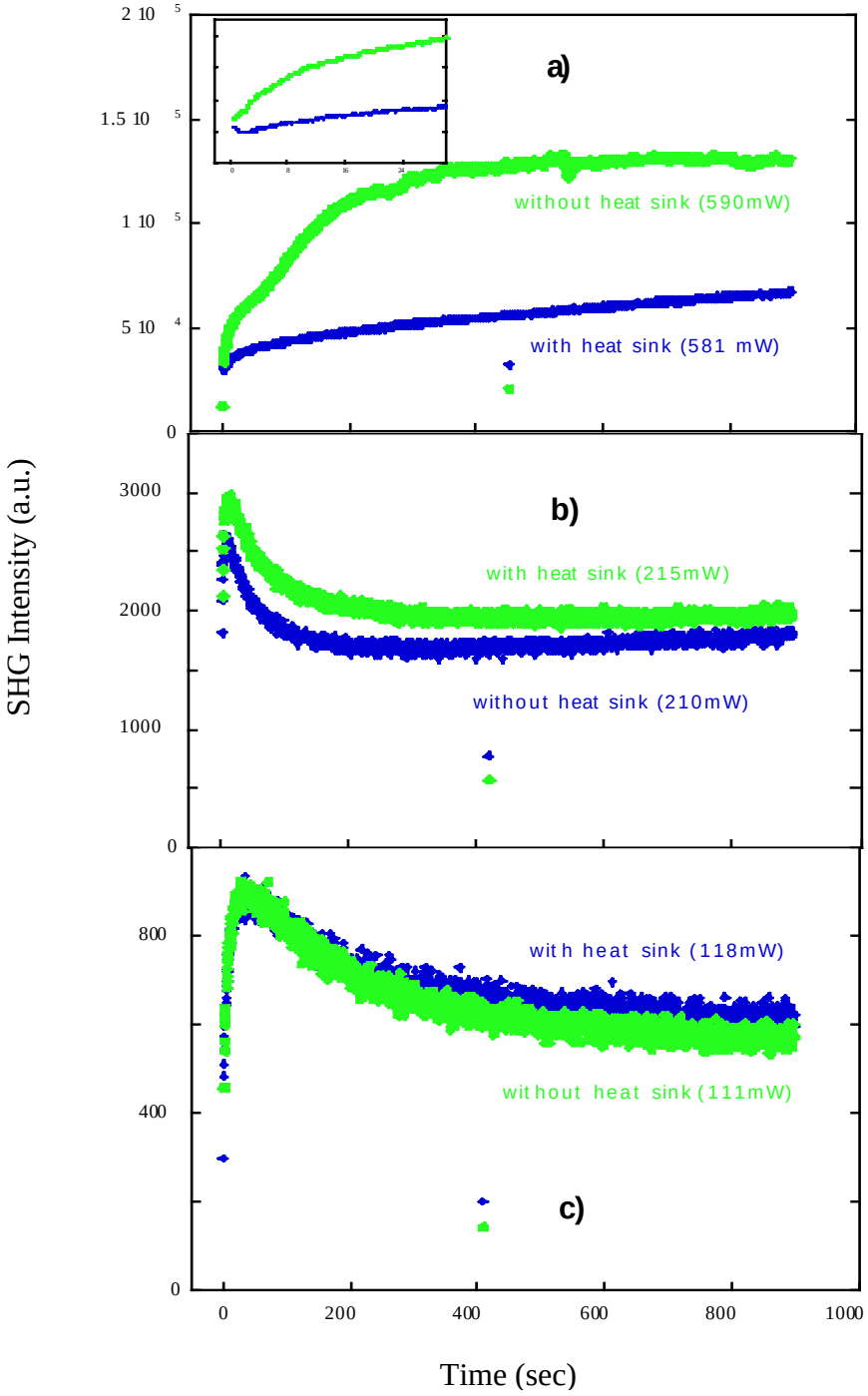

Fig. 3.12 SHG from Si-ZrSiOx with various laser intensities. a) 580 mW, b) 210 mW, c) 110 mW. The inset in (a) is the enlargement of measurement a for the first 36 seconds.

greatly curtailed when the heat sink is put in place. (The decrease in SHG also reappears even at very high power as the inset in fig 3.12a shows.) This strongly indicates that at high laser incident intensity, the monotonic increase in SHG signal over the entire measurement time is due to a gradual increase in the temperature of the sample caused by the incident laser. As the power of the laser is reduced, this effect becomes less and less pronounced. It has essentially no effect at low power (fig 3.12c), which is the power range used in earlier measurements. This indicates that the effect observed in fig 3.6 is not due to temperature.

SHG increase caused by increasing temperature has been observed in Si-SiO_2 system. [Dadap 1995] It is believed to be caused by thermoelastic strain, which arises from the differences in the thermal expansion rates of the oxide layer and the substrate. The strain, normal to the surface, creates a local structural gradient at the Si-SiO_2 interface, which acts as an additional nonlinear polarization sources. In our experiments, since the physical thickness of the $ZrSiO_x$ layer is much larger than the ultra thin SiO_2 layer, the strain caused by the thermal expansion difference is also much larger, which then dominates the SHG signals.

There can be another factor that contributes to the large temperature effect in Si-$ZrSiO_x$ system. $ZrSiO_x$ is a composite of SiO_2 and ZrO_2 with no bonds between Si and Zr. [Blumenthal 1958] An atomic model for $ZrSiO_4$ is shown in figure 3.13. As Fig. 3.13 shows, the $ZrSiO_4$ material consists of chains of ZrSiO. There are also bonds between Zr atoms at one chain and O atoms at nearby chains. This makes the structure to be stable in three dimensions.

As the temperature rises, the bonds between those chains are weakened and may break. This results in strains, traps and defects at the interface that breaks symmetry. This then leads to an increase in SHG signal.

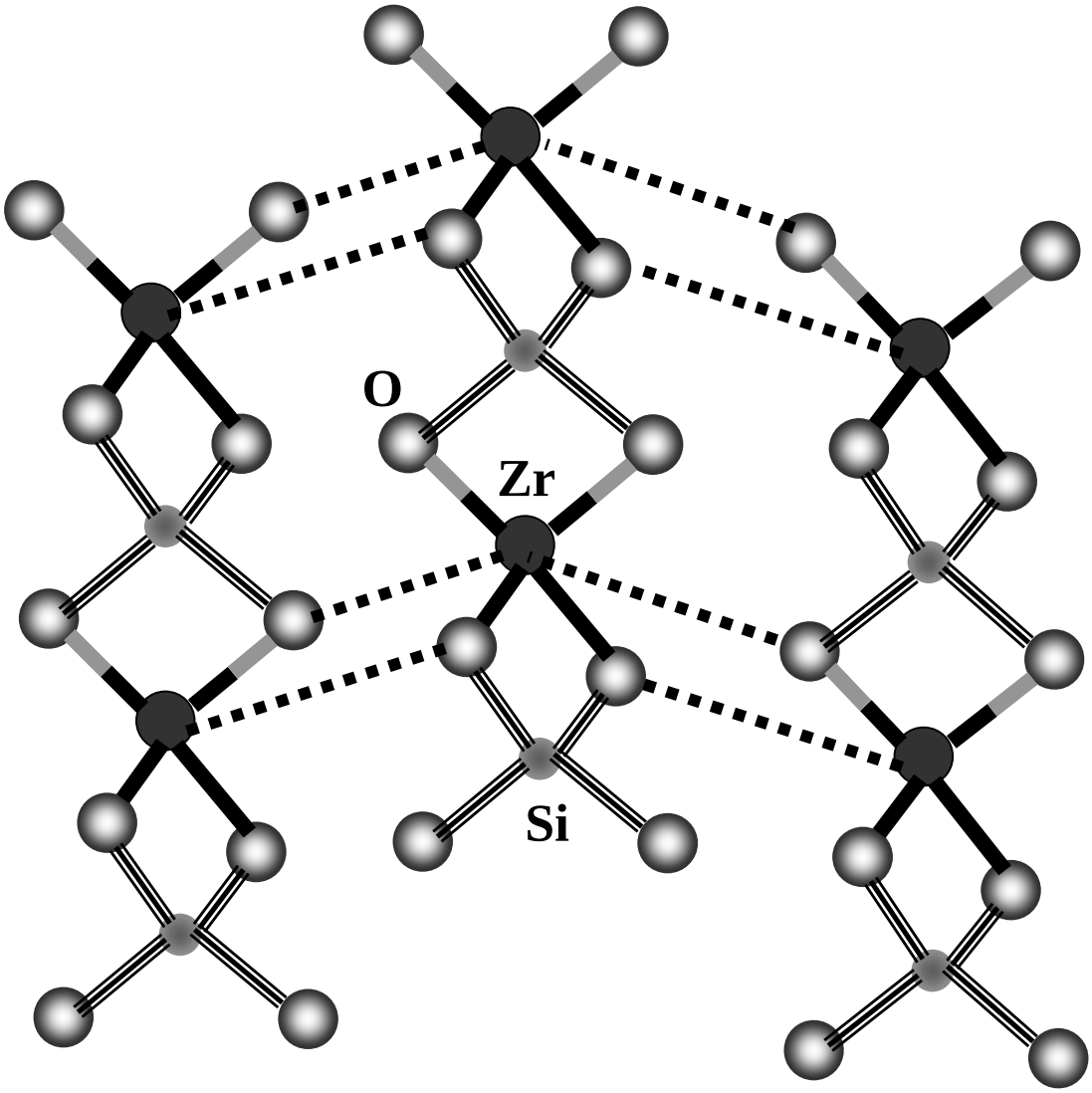

Figure 3.13 Atomic structure of SiO_2-ZrO_2. (After [Wilk 2000])

CHAPTER IV

SUMMARY

IV.1 Summary

This dissertation describes research on the application of intense, tunable, ultrafast lasers to studies of the silicon-dielectric system. Among the nonlinear optical effects, second harmonic generation (SHG) has come to be recognized as a uniquely useful tool. SHG is sensitive to interfaces between materials with inversion symmetry. This technique can then yield rich information on electronic structure, local fields, symmetry and carrier dynamics at interfaces. It also has the advantages of being contactless, non-intrusive and is easily applicable to *in situ* measurements. It is therefore a promising tool for investigation of mature Si-dielectric interfaces.

In this thesis, we use the SHG technique to study the interfaces between silicon and dielectrics, including both the mature Si-SiO_2 system and the newly developed Si-$ZrSiO_x$ (high-k) system.

In Si-SiO_2 system, we show the first definite evidence for the three-photon electron injection from the silicon conduction band to the conduction band of the silicon dioxide. A thickness threshold for the electron tunneling of about 20 Å is also observed.

In particularly we present first SHG measurements of the Si-high-K dielectric material system. Our data show features that are drastically different from that of the Si-SiO_2 system. Unlike the Si-SiO_2 system, where a rapid initial rise in SHG intensity is followed by a gradual increase until saturation, SHG from Si-$ZrSiO_x$ gradually decreases to a stable level after an initial quick rise. We attribute this difference to different carrier dynamics in these two systems. While in the SiO_2 system, electron injection dominates the process, holes and electrons have a much more equal role in $ZrSiO_x$. This arises from characteristically different band structures in these two systems. Wavelength-dependent measurements of the SHG from Si/$ZrSiO_x$ are also performed. A threshold of about 1.4 eV for electron injection is observed. From these measurements, a band diagram at the Si-$ZrSiO_x$ interface can be constructed showing band offsets. According to this diagram, the values of both valence band offset (~3.2 eV) and

conduction band offset (~2.8 eV) are both reasonably large, which can prevent hot carrier tunneling at the interface. This gives strong support to $ZrSiO_x$'s candidacy as a replacement for SiO_2 in future generation semiconductor devices.

At high laser power, it is also observed that the SHG intensity monotonically increases with time. This effect is believed to be of thermal origin. A temperature rise can lead to stress and broken bonds, which can cause an increase in SHG. The atomic structure of $ZrSiO_4$, which consists of Zr-O-Si chains, is consistent with this explanation.

IV.2 Ongoing Work and Future Plan

This dissertation illustrates the successful use of the SHG technique to study both Si-SiO_2 and Si-$ZrSiO_x$ systems. The potential of this technique is yet to be fully utilized and its applications to other systems just start to be explored.

In Si-$ZrSiO_x$ system, the composites of SiO_2 and ZrO_2 affect many properties of the system including the band gap of $ZrSIO_x$ and the band offsets at the Si/$ZrSIO_x$ interface. Based on the model we proposed in this thesis work, SHG measurements can be used to investigate these changes.

Diamond has a band gap of about 6 eV, close to the band gap of $ZrSiO_x$ used in our experiments. The mobility of holes in diamond is also comparable to electrons. These properties suggest SHG measurements performed on diamond-silicon system may show strong signs of hole injection. Some preliminary SHG experiments seem to be consistent with this suggestion. More systematic studies on this system not only can yield more information about the carrier dynamics at the diamond-silicon interface, but also will provide important information for the efforts to establish EFISH as a standard tool for thin film analysis.

Some preliminary experiments have also been done on other systems. In the AlGaSb/InAs quantum wells, EFISH measurements show the existence of a strong internal electric field. This field has been indirectly detected by other methods. The results from the SHG experiment are the first direct evidence for the existence of this internal electric field.

Crystalline oxides on silicon (COS) are the most recent approach to tackle the gate oxide problem. Some preliminary SHG experiments have been done with the $SrTiO_3$-Si system. A threshold near 8500 Å (1.37 eV) is observed. The exact nature of this threshold is still unclear.

Radiation effects on silicon devices have been an important topic for many years. Our preliminary results again show that the SHG techniques can be a sensitive tool to detect impacts from radiation, especially for silicon with ultra-thin oxides, which are not easily available to electrical measurements.

Silicon on insulator (SOI) is another direction being pursued by many researchers. It is believed by some people to be the path to the future generations of semiconductor technology. The SHG technique once again detects differences between hydrogenated SOI and non-hydrogenated SOI.

This dissertation is a pioneering effort to establish the second-harmonic-generation technique as an alternative method to characterize the electronic and atomic structures at the Si-dielectric interfaces. More quantitative work with SHG will be the direction of future research.

APPENDIX A

NONLINEAR SUSCEPTIBILITY OF THE CLASSICAL ANHARMONIC OSCILLATOR MODEL

The classical Lorentz model of the atom, which treats the atom as a harmonic oscillator, is proven to be successful in describing linear optical properties such as dispersion and resonance absorption. This model can be extended by introducing nonlinearity in the restoring force exerted on the electron. The primary shortcoming of this classical model is that it ascribes a single resonance frequency (ω_o) to each atom. Therefore, it cannot describe the complete resonance nature of the nonlinear susceptibility, such as the possibility of simultaneous one- and two-photon resonance. In contrast, the quantum mechanical theory of the nonlinear optical susceptibility can adequately address such issues.

A.1 Classical Harmonic Oscillator (Lorentz Model)

When an atom is in an electric field, the electrons and the positively charged ion core experience forces with opposite direction. Therefore when an electromagnetic wave interacts with a material, the atoms in the materials turn into electric dipoles as their electrons and ion cores move in opposite directions. In the Lorentz model, the ion core has infinite mass and does not move. The electron is bound to the massive ion core and oscillates in a perfect harmonic potential, which has the form of

$$\mathbf{U(x) = \frac{1}{2} m\omega_0^2 x^2} \qquad \textbf{(A-1)}$$

where m is the mass of the electron, ω_o is the resonance frequency and x is the distance between the electron and the ion core. The equation of motion then is

$$\mathbf{\ddot{x} + \Gamma\dot{x} + \omega_0^2 x = -\frac{eE(t)}{m}} \qquad \textbf{(A-2)}$$

where Γ designates the damping rate.

Assuming the electromagnetic wave is a plane wave with frequency ω,

$$\mathbf{E(t) = E_0(e^{-i\omega t} + e^{i\omega t})} \qquad \textbf{(A-3)}$$

where E_0 is real, then the steady state solution to (A-2) is of the form

$$\mathbf{x(t) = x_0 e^{-i\omega t} + x_0^* e^{i\omega t}} \qquad \textbf{(A-4)}$$

where x_0^* is the complex conjugate of x_o.

By inserting (A-4) into equation (A-2), one can find:

$$\mathbf{x_0 = -\frac{eE_0}{mD(\omega)}} \qquad \textbf{(A-5a)}$$

where $$\mathbf{D(\omega) = \omega_0^2 - \omega^2 - i\omega\Gamma} \qquad \textbf{(A-5b)}$$

The electron oscillates at the same frequency of the incident electromagnetic wave. The resulting oscillating dipole then emits radiation at the same frequency as well.

The electric dipole moment of an electron is given by $p=ex$. Suppose that there are N molecules per unit volume and Z electrons per molecule. And for each molecule, there are f_j electrons with resonance frequency ω_j and damping rate Γ_j. The summation of all electron dipole moments in the material gives the polarization P,

$$\begin{aligned}\mathbf{P(\omega)} &= \mathbf{\sum_{all} -ex = \frac{Ne^2}{m}\sum_j f_j\left(\frac{e^{-i\omega t}}{D_j(\omega)} + C.C.\right)E_0} \\ &= \mathbf{\frac{Ne^2}{m}\sum_j f_j\left(\frac{e^{-i\omega t}}{\omega_j^2 - \omega^2 - i\omega\Gamma_j} + C.C.\right)E_0}\end{aligned} \qquad \textbf{(A-6a)}$$

where C.C. stands for complex conjugate and the summation of j satisfies

$$\mathbf{\sum_j f_j = Z} \qquad \textbf{(A-6b)}$$

It shows the linear optical response to the incident electromagnetic field. The familiar linear electric susceptibility χ can then be found as

$$\mathbf{\chi^{(1)} = \frac{Ne^2}{m}\sum_j \frac{f_j}{D_j(\omega)} = \frac{Ne^2}{m}\sum_j \frac{f_j}{\omega_j^2 - \omega^2 - i\omega\Gamma_j}} \qquad \textbf{(A-7)}$$

A.2 Nonlinear Susceptibility of a Classical Anharmonic Oscillator

When the incident electromagnetic field is large, the displacements of the electrons from their equilibrium positions can be large enough that the potential experienced by the electrons deviates from the parabola function. However if the deviation is not very large, the anharmonic terms in the potential can be expanded in a power series:

$$\mathbf{U_{anharmonic} = \frac{1}{3}max^3 + \frac{1}{4}mbx^4 + ...} \qquad \textbf{(A-8)}$$

If only the first two terms in (A-8) are considered, the equation of motion for the electron now takes the form of:

$$\mathbf{\ddot{x} + \Gamma\dot{x} + \omega_0^2 x + ax^2 + bx^3 = -\frac{eE(t)}{m}} \qquad \textbf{(A-9)}$$

Suppose the incident electromagnetic wave *E(t)* still takes the form of (A-3). Although no general solution to (A-9) can be found, one can analyze the response of the oscillator by expanding the displacement *x(t)* in powers of the electric field *E(t)*.

$$\mathbf{x(t) = x^{(1)}(t) + x^{(2)}(t) + x^{(3)}(t) + ...} \qquad \textbf{(A-10)}$$

where $x^{(i)}(t)$ is proportional to the *i*-th power of the field *E(t)*.

Inserting (A-10) into (A-9), one has

$$\begin{aligned}
&\mathbf{\ddot{x}^{(1)} + \ddot{x}^{(2)} + \ddot{x}^{(3)} + \Gamma\dot{x}^{(1)} + \Gamma\dot{x}^{(2)} + \Gamma\dot{x}^{(3)} + \omega_0^2 x^{(1)} + \omega_0^2 x^{(2)} + \omega_0^2 x^{(3)}} \\
&\mathbf{+ a\{(x^{(1)})^2 + (x^{(2)})^2 + (x^{(3)})^2 + 2x^{(1)}x^{(2)} + 2x^{(1)}x^{(3)} + 2x^{(2)}x^{(3)}\}} \\
&\mathbf{+ b\{(x^{(1)})^3 + (x^{(2)})^3 + (x^{(3)})^3 + 6x^{(1)}x^{(2)}x^{(3)} + 3(x^{(1)})^2 x^{(2)} + 3(x^{(1)})^2 x^{(3)}} \\
&\mathbf{+ 3(x^{(2)})^2 x^{(3)} + 3(x^{(2)})^2 x^{(1)} + 3(x^{(3)})^2 x^{(1)} + 3(x^{(3)})^2 x^{(2)}\} = -\frac{eE(t)}{m}}
\end{aligned} \qquad \textbf{(A-11)}$$

If the deviation in the displacement *x(t)* is small, only terms up to the third power of E(t) need to be considered. And if (A-11) holds for all fields, terms with the same power of *E(t)* on both side of the equator have to be equal. This leads to equations for the first, second, and third power of *E(t)*:

$$\mathbf{\ddot{x}^{(1)} + \Gamma\dot{x}^{(1)} + \omega_0^2 x^{(1)} = -\frac{eE(t)}{m},} \qquad \textbf{(A-12a)}$$

$$\mathbf{\ddot{x}^{(2)} + \Gamma\dot{x}^{(2)} + \omega_0^2 x^{(2)} + a(x^{(1)})^2 = 0} \qquad \textbf{(A-12b)}$$

$$\mathbf{\ddot{x}^{(3)} + \Gamma\dot{x}^{(3)} + \omega_0^2 x^{(3)} + 2ax^{(1)}x^{(2)} + b(x^{(1)})^3 = 0} \qquad \textbf{(A-12c)}$$

Equation (A-12a) is just the linear equation of motion for a harmonic oscillator. Its solution is shown in (A-4) and (A-5). Therefore one can solve $x^{(1)}$:

$$\mathbf{x^{(1)}(t) = x_0^{(1)} e^{-i\omega t} + C.C. = -\frac{eE_0}{mD(\omega)} e^{-i\omega t} + C.C.} \qquad \textbf{(A-13)}$$

Inserting (A-13) into it (A-12b) and treating $a(x^{(1)})^2$ as an inhomogeneous driving term just like *–eE(t)/m*, one can obtain the lowest nonlinear correction term for *x(t)*.

$$\ddot{x}^{(2)} + \Gamma\dot{x}^{(2)} + \omega_0^2 x^{(2)} = -a(x^{(1)})^2$$
$$= -a\{(x_0^{(1)})^2 e^{-i\omega t} + (x_0^{(1)*})^2 e^{-i\omega t} + 2x_0^{(1)}x_0^{(1)*}\} \quad \textbf{(A-14)}$$

The square of $x^{(1)}(t)$ leads to the double frequency 2ω, second harmonic generation (SHG), and a DC-like component, optical rectification (OR). The solution to (A-14) has the form of

$$x^{(2)}(t) = x_0^{(2)} e^{-i2\omega t} + x_0^{(2)*} e^{i2\omega t} + x^{(2)}(\omega = 0) \quad \textbf{(A-15)}$$

with

$$x_0^{(2)} = -\left(\frac{e}{m}\right)^2 \frac{aE_0^2}{D(2\omega)D^2(\omega)} \quad \textbf{(A-16a)}$$

$$x^{(2)}(\omega = 0) = -\left(\frac{e}{m}\right)^2 \frac{2aE_0^2}{D(0)|D(\omega)|^2} \quad \textbf{(A-16b)}$$

Following the definition of polarization in (A-6), one finds the expression for the second-order nonlinear term of the polarization.

$$P(\omega) = \sum_{all} -ex = \frac{Ne^3}{m^2} \sum_j f_j \left(\frac{a_j e^{-i2\omega t}}{D_j(2\omega)D_j^2(\omega)} + C.C. \right) E_0^2 \quad \textbf{(A-17)}$$

The second order electric susceptibility then will be

$$\chi^{(2)} = \frac{Ne^3}{m^2} \sum_j \frac{f_j a_j}{D_j(2\omega)D_j^2(\omega)} \quad \textbf{(A-18)}$$

After solving $x^{(2)}$, one can insert it and $x^{(1)}$ into (A-12c) and solve for $x^{(3)}$. The solution to (A-12c) will lead to third harmonic generation (THG).

A.3 Centrosymmetric Materials

The discussion so far does not take the symmetry of the materials into account. When the material under consideration possesses inversion symmetry, certain restrictions apply to the nonlinear polarization.

Under inversion symmetry, potential energy U(x) satisfies U(x)=U(-x). Therefore all the odd order anharmonic terms in the potential energy (A-8) vanish. The equation of motion for an anharmonic oscillator will then have the form of

$$\ddot{x} + \Gamma\dot{x} + \omega_0^2 x + bx^3 = -\frac{eE(t)}{m} \quad \textbf{(A-19)}$$

As having done previously, one can expand the displacement *x(t)* in the power series of *E(t)*, insert the power series into (A-19), and equate like powers of *E(t)*. This gives the group of equations:

$$\ddot{\mathbf{x}}^{(1)} + \Gamma\dot{\mathbf{x}}^{(1)} + \omega_0^2\mathbf{x}^{(1)} = -\frac{\mathbf{eE(t)}}{\mathbf{m}}, \qquad \textbf{(A-20a)}$$

$$\ddot{\mathbf{x}}^{(2)} + \Gamma\dot{\mathbf{x}}^{(2)} + \omega_0^2\mathbf{x}^{(2)} = \mathbf{0} \qquad \textbf{(A-20b)}$$

$$\ddot{\mathbf{x}}^{(3)} + \Gamma\dot{\mathbf{x}}^{(3)} + \omega_0^2\mathbf{x}^{(3)} + \mathbf{b}(\mathbf{x}^{(1)})^3 = \mathbf{0} \qquad \textbf{(A-20c)}$$

The second equation (A-20b), which gives second harmonic generation, now has no driving terms but only a damping term. This means its steady state solution vanishes.

$$\mathbf{x^{(2)}=0} \qquad \textbf{(A-21)}$$

Therefore in the centrosymmetric materials, second harmonic generation is forbidden under electric dipole approximation. It is easy to see that all the even order nonlinearity in the centrosymmetric materials vanish as well.

It is also clear from (A-20c), the third order nonlinearity still exists in the centrosymmetric materials.

REFERENCES

[Aktsipetrov 1984] O. A. Aktsipetrov and E. D. Mishina, Sov. Phys. Dokl. 29 (1984) 37

[Aktsipetrov 1996] O. A. Aktsipetrov, A. A. Fedyanin, E. D. Mishina, A. N. Rubtsov, C. W. van Hasselt, M. A. C. Devillers, and Th. Rasing, Phys. Rev. Lett., 54, (1996) 1825

[Aktsipetrov 1999] O. A. Aktsipetrov, A. A. Fedyanin, A. V. Melnikov, E. D. Mishina, A. N. Rubtsov, M. H. Anderson, P. T. Wilson, M. ter Beek, X. F. Hu, J. I. Dadap, and M. C. Downer, Phys. Rev. B, 60 (1999) 8924

[Balk 1988] P. Balk in P. Balk (ed.) *The Si-SiO_2 system*, (Elsiever, Amsterdam, 1988)

[Blumenthal 1958] W. B. Blumenthal, *The Chemical Behavior of Zirconium*, (van Nostrand, Princeton, 1958), p. 201-219

[Cardona 1966] M. Cardona and F. H. Pollak, Phys. Rev., 142 (1966) 530

[Daum 1993] W. Daum, H. –J. Krause, U. Reichel, and H. Ibach, Phys. Rev. Lett., 71 (1993) 1234

[Berglund 1971] C. N. Berglund and R. J. Powell, J. Appl. Phys., 42 (1971) 573

[Bloch 1996] J. Bloch, J. G. Mihaychuk, and H. M. van Driel, Phys. Rev. Lett., 77 (1996) 920

[Campbell 1997] S.A. Campbell, D. C. Gilmer, X. Wang, M. Hsieh, H. Kim, W. L. Gladflter, and J. Yan, IEEE Trans. Electron Dev., 44 (1997) 104

[Caplan 1982] Philip J. Caplan and Edward H. Poindexter, J. Appl. Phys., 53 (1982) 541

[Cernusca 1998] M. Cernusca, R. Heer, and G. A. Reider, Appl. Phys. B, 66 (1998) 367

[Cerullo 1994] G. Cerullo, S. De Silvestri, V. Magni, and L. Pallaro, Opt. Lett., 19, (1994) 807

[Dadap 1995] J. I. Dadap, X. F. Hu, N. M. Russell, J. G. Ekerdt, J. K. Lowell, and M. C. Downer, IEEE J. Sel. Topics Quantum Electron., 1 (1995) 1145

[Dadap 1996] J. I. Dadap, X. F. Hu, M. H. Anderson, and M. C. Downer, Phys. Rev. B, 53 (1996) R7607

[Daschbach 1995] J. L. Daschbach, P. R. Fischer, D. E. Gragson, D. Demarest, and G. L. Richmond, J. Phys. Chem., 99 (1995) 3240

[Ducasse 1998] A. Ducasse, C. Rullière, and B. Couillaud in C. Rullière (ed.), *Femtosecond laser Pulses*, (Springer, Berlin, 1998), pg. 56

[Fathauer 1984] R. W. Fathauer and L. J. Schowalter, Appl. Phys. Lett., 45 (1984) 519

[Feldman 1998] L. C. Feldman, E. P. Gusev, and E. Garfunkel in E. Garfunke, E. Gusev, and A. Vul' (ed.), *Fundamental Aspects of Ultrathin Dielectrics on Si-based Devices*, (Kluwer, Dordrecht, 1998)

[Fork 1984] R. L. Fork, O. E. Martinez, and J. P. Gordon, Opt. Lett., 9, (1984) 150

[Franken 1961] P. A. Franken, A. E. Hill, C. W. Peters, and G. Weinreich, Phys. Rev. Lett., 7, (1961) 118

[Godefroy, 1996] P. Godefroy, W. de Jong, C. W. van Hasselt, M. A. C. Devillers, and Th. Rasing, Appl. Phys. Lett., 68 (1996) 1981

[Guyot-Sionnest 1988] P. Guyot-Sionnest and Y. R. Shen, Phys. Rev. Lett., 38 (1988) 7985

[Hattangady 1995] S. V. Hattangady, H. Niimi, and G. Lucovsky, Appl. Phys. Lett., 66 (1995) 3495

[Heil 1935] O. Heil, US Patent 439, 457, 1935

[Heinz 1985] T. F. Heinz, M. M. T. Loy, and W. A. Thompson, Phys. Rev. Lett., 54 (1985) 63

[Hwang 1990] Hyunsang Hwang, Wenchi Ting, Bikas Maiti, Dim-Lee Kwong, and Jack Lee, Appl. Phys. Lett., 57 (1990) 1010

[Ishiwara 1982] H. Ishiwara and T. Asano, Appl. Phys. Lett., 40 (1982) 66

[Ito 1982] T. Ito, T. Nakamura and H. Ishikawa, IEEE Trans. Electron. Devices, 29 (1982) 498

[Kizilyalli 1998] I. C. Kizilyalli, R. Y. S. Huang, and P. K. Roy, IEEE Electron Dev. Lett., 19 (1998) 423

[Koechner 1996] W. Koechner, *Solid-state laser engineering* 4th edition, (Springer, Berlin, 1996)

[Krueger 1993] J. Krueger, N. Sorg, J. Reif, and W. Kautek, Appl. Surf. Sci., 69 (1993) 388

[Kumar 1972] Arun Kumar, Dilip Rajdev, and D. L. Douglass, J. Am. Cera. Soc., 55 (1972) 439

[Lautenschlager 1987] P. Lautenschlager, M. Garriga, L. Viña, and M. Cardona, Phys. Rev. B, 36 (1987) 4821

[Lee 1967] C. H. lee, R. K. Chang, and N. Bloembergen, Phys. Rev. Lett., 18, (1967) 167

[Lunsford 1973] J. H. Lunsford, Catal. Rev. 8, (1973) 135

[Lüpke 1995] G. Lüpke, C. Meyer, C. Ohlhoff, H. Kurz, S. Lehmann, and G. Marowsky, Opt. Lett., 20 (1995) 1997

[McGilp 1986] J. F. McGilp and Y. Yeh, Solid State Commum., 59 (1986) 91

[McGilp 1996] J. F. McGilp, J. Phys. D, 29 (1996) 1812

[McKee 1998] R. A. McKee, F. J. Walker, and M. F. Chisholm, Phys. Rev. Lett., 81 (1998) 3014

[Mihaychuk 1995] J. G. Mihaychuk, J. Bloch, and H. M. van Driel, Opt. Lett., 20 (1995) 2063

[Nahata 1996] A. Nahata, J. A. Misewich, and T. F. Heinz, Appl. Phys. Lett., 69 (1996) 746

[Oldham 1986] T. R. Oldham, A. J. Lelis, and F. B. McLean, IEEE Tans. Nucl. Sci., NS-33 (1986) 1203

[Ohlhoff 1996] C. Ohlhoff, C. Meyer, G. Lüpke, T. Löffler, T. Pfeifer, H. G. Roskos, and H. Kurz, Appl. Phys. Lett., 68 (1996) 1699

[Parker 1998] C.G. Parker, G. Lucovsky, and J. R. Hauser, IEEE Electron Dev. Lett., 19 (1998) 106

[Sarger 1998] L. Sarger and J. Oberlé in C. Rulliére (ed.), *Femtosecond Laser Pulses*, (Spinger, Berlin, 1998) p.177

[Shamir 2000] N. Shamir, J. G. Mihaychuk, and H. M. van Driel, J. Appl. Phys., 88 (2000) 896

[Shen 1985] J. Vac. Sci. Technol. B, 3 (1985) 1464

[Sipe 1987] J. E. Sipe, D. J. Moss, and H. M. van Driel, Phys. Rev. Lett., 35 (1987) 1129

[Sjodin 1998] Theodore Sjodin, Hrvoje Petek, and Hai-Lung Dai, Phys. Rev. Lett., 81 (1998) 5664

[Spence 1991] D. E. Spence, P. N. Kean, and W. Sibbett, Opt. Lett., 16 (1991) 42

[Svensson 1988] Svensson in P. Balk (ed.) *The Si-SiO_2 system*, (Elsiever, Amsterdam, 1988) p. 223

[Sze 1981] S. M. Sze, *Semiconductor devices, physics and technology* 2nd edition, (Wiley, New York, 1981)

[Tauber 1971] R. N. Tauber, A. C. Dumbri, and R. E. Caffrey, J. Electronchem. Soc., 118 (1971) 747

[Terhune 1962] R. W. Terhune, P. D. Maker, and C. M. Savage, Phys. Rev. Lett., 8, (1962) 404

[Tom 1984] H. W. K. Tom, C. M. Mate, X. D. Zhu, J. E. Crowell, T. F. Heinz, G. A. Somorjai, and Y. R. Shen, Phys. Rev. Lett., 52 (1984) 348

[Wang 1988] S. Q. Wang and J. W. Mayer, J. Appl. Phys., 64 (1988) 4711

[Wilk 2000] G. D. Wilk, R. M. Wallace, and J. M. Anthony, J. Appl. Phys., 87 (2000) 484

[Wolfe 1999] D. M. Wolfe, *Thermochemical stability of silicon oxycarbide, SiO_xC_y ($x,y \leq 0.2$), and zirconium silicate, $(ZrO_2)_x$-$(SiO_2)_{1-x}$ ($x \leq 0.5$), thin films deposited via remote plasma enhanced chemical vapor deposition (RPECVD)*, PhD Dissertation, (North Carolina State University, 1999)